DEVELOPMENT OF SWITCHABLE SPIN SELECTIVITY BASED ON CONTROLLABLE ORGANIC CHIRALITY

RUTTAPOL MALATONG

THE GRADUATE UNIVERSITY FOR ADVANCED STUDIES, SOKENDAI

INSTITUTE FOR MOLECULAR SCIENCE

SCHOOL OF PHYSICAL SCIENCES

DEPARTMENT OF STRUCTURAL MOLECULAR SCIENCE

2023

Development of Switchable Spin Selectivity Based on Controllable Organic Chirality

Abstract

RUTTAPOL MALATONG

A chiral symmetry, an ultimate form of broken symmetry lacking both inversion and mirror symmetries, has recently attracted growing interest due to its unique ability to compellingly tie the electron motion to its spin angular momentum. A recent striking example is a gigantic spin-polarized current that emerged in organic chiral molecules, which is often referred to as chiral-induced spin selectivity (CISS). The phenomenon is noticeable in that pure organic systems give a platform of the CISS with light elements where a spin-orbit interaction (SOI) is negligibly small. Conversely, a conventional charge-to-spin conversion such as the Edelstein effect is well associated with a large SOI in a heavy-element system. Although the microscopic origin of the unexpectedly large spin polarization of CISS is still controversial, the CISS effect potentially paves the way to a novel method of embedding organic chiral materials into solid-state spintronic and optical devices.

Because most of the chiral materials used in the CISS experiment-based solid-state devices are static molecules, in which the handedness molecules are fixed by their chemical bonds which are unable to invert spin polarization (SP) direction, spin polarization (SP) direction manipulation by efficiently controlling the chiral handedness with external excitation in “single device’’ has yet to be intensively studied to date. In this thesis, developing switchable organic molecules with external controllability, capable of inversion of spin polarization, is highly desired to study challengingly. It is anticipated that this switchable organic molecule would allow for constructing the responsive spintronic devices as well as representing a huge step forward in the field of organic spintronic applications.

Therefore, considerable interest in CISS lies in switchable chiral molecules with external controllability as first presented in a chapter **“(i) Highly Durable Spin Filter Switching Based on Self-Assembled Chiral Molecular Motor”**. By studying molecular motors known as

overcrowded alkenes (OCAs), their handedness are switched by light irradiation and heat treatments. In a previous study, OCA-based devices that exhibit CISS remains far from completion in terms of practical use, and rather fundamental obstacles such as (i) external controllability of spin, (ii) function durability, and (iii) improvement of spin-polarization efficiency have yet to be surmounted. Therefore, I aim to prepare new molecular systems based on overcrowded alkene that can address the three obstacles mentioned above to develop the practical utilization of CISS effect. I developed a self-assembled monolayer (SAM) of overcrowded alkene (OCA)-based molecular motor. With this system, I successfully demonstrate that the direction of spin polarization can be externally and repeatedly manipulated in an extremely stable manner by switching the molecular chirality, which is achieved by a formation of the covalent bonds between the molecules and electrode. In addition, by focusing on the stereo architecture of the SAM of the OCAs, I pursue a new route to enhance the spin polarization efficiency per a single OCA molecule. The present experimental investigations report the creditable feasibility study towards the versatile CISS-based spintronic molecular devices with controllability, durability, and high efficiency.

Thus far, most CISS studies have intensively focused on chiral metals or insulating organic monomolecular layers to experimentally discuss spin-polarized current. Then a fundamental question arises on CISS effect in chiral ferroelectric materials because charge transport in macroscopic ferroelectric materials is only possible with displacement current. Therefore, an emergent spin-polarized current, if any, is likely due to the displacement current. In the second work, my significant research interest focuses on chiral dielectric materials as triglycine sulfate (TGS) **"(ii) Engineering Surface Spin Based on Chiral dielectric Materials''**.

Triglycine sulfate (TGS) crystal consists of achiral phase above transition temperature, and it will be chiral phase below transition temperature. A unique handedness can be characterized throughout the entire crystal by poling process (decreasing temperature from the achiral high-temperature phase) with electric field parallel to the (polar) y-axis. Thus, it is reasonable to hypothesize the CISS in TGS after poling, which can be measured as spin accumulation. Since TGS has demonstrated magnetochiral anisotropy (MChA) in a previous report, the interplay between chirality and magnetism also opens a whole new window on this material. I studied alternating current (AC)-induced CISS effect in TGS under AC current excitation by detecting the

spin accumulation with direct current (DC) voltage at the interface. The results demonstrate the antisymmetric signal profiles with temperature dependence close to transition temperature (321.7 K) as the function of the magnetic field. Unfortunately, the TGS-based devices with different handedness, switched by an opposite poling process, exhibit similar behavior. This phenomenon is not likely due to CISS, in which spin accumulation could not be detected, even if the chirality is switched. In this thesis, the possible antisymmetric curves and why CISS undetected will be discussed in detail.

Acknowledgement

This Ph.D. thesis is the achievement of dedication, effort, and passion that I am so proud of. My Ph.D. study, however, would not have been successful without numerous people.

Words cannot express my enormous appreciation to my supervisor, Professor Hiroshi M. Yamamoto, for all the invaluable patience and feedback with profound knowledge throughout my Ph.D. study. It was a great honor to have him as my supervisor because My Ph.D. journey would not have been smooth and productive without him for his valuable guidance and help.

I also could not have undertaken this journey without great help and precious guidance from Assistant Professor Takuro Sato. I am delighted to work with him, in which he always promptly helped to drive my research effectively. Also, many thanks to the Yamamoto lab members for all their support and help in both working time and daily time in Japan.

I would also like to warmly thank my family: parents and brother, for always supporting and being by my side throughout my life decision. Lastly, Thanks can never enough show my appreciation to my best and lovely friends: Rhine, May, Tann, Long, Cici, and Lee, who have been my great moral support and made Japan my second home.

Ruttapol MALATONG

2023 July 11

Contents

Chapter 1

Introduction

1.1 The overview of chiral-induced spin selectivity (CISS) effect

Spin-orbit interaction (SOI) is the interaction of electron spin with its orbital motion that induces spin-dependent polarization at the fermi surfaces. SOI is one of the most intriguing sources for providing a variety of electronic functionalities. Conversion of charge-to-spin, that is related with a huge SOI, for example, Rashba SOI, due to a heavy-element system plays a crucial role in locking of spin polarization direction and momentum referred to as spin momentum locking (see in Fig. 1.1).[1–6] In terms of symmetry languages,[7] Rashba system is lacking inversion symmetry. The spins are reversed when spins and mirror plane are parallel. Whereas the spins are the same when spins and mirror plane are perpendicular. With this system, the spins are perpendicularly locked to the electron momentum (see in Fig. 1.1a). Under electric field, spin-dependent Fermi surfaces are shifted to form a finite spin density, inducing spin polarization perpendicular to the electron velocity. However, the above relation breaks down if both inversion and mirror symmetry are broken which are remarkably observed in the chiral system. Fig. 1.1b depicts the spin-dependent Fermi surfaces pointing inwards or outwards that are parallel to the electron velocity, depending on the chirality. Under electric field, the spin-dependent Fermi surfaces are shifted, consequently the spins are polarized in (anti)parallel with the positive (negative) current in the right-handed system. On the one hand, the polarization gets reversed in the left-handed.

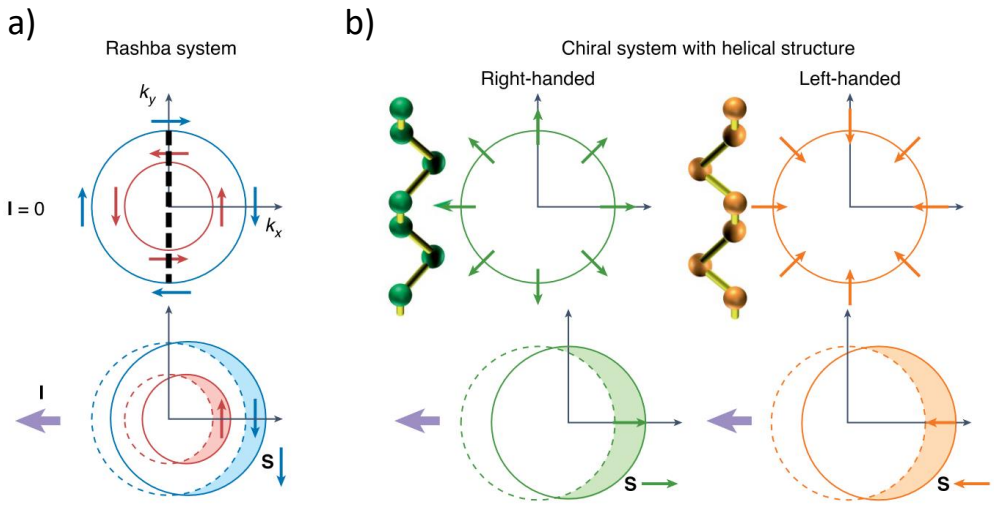

Fig. 1.1 a) schematic of spin momentum locking a) Rashba systems and b) chiral systems. The circles represent Fermi surfaces, and arrows around the circles represent spins, respectively, in the reciprocal space k (k_x, k_y, k_z) of crystal structures with current I.[7]

A similar but different recent striking example has been observed in the context of spin momentum locking in chiral system that is called chiral-induced spin selectivity (CISS), which generates a gigantic spin-polarization emerged in organic chiral molecules.[8–13] In the CISS experiment, when electrons transmit through the chiral system such as DNA, α-helix polypeptide, or chiral amino acid, electrons become spin-polarized in (anti)parallel directions to the electron's velocity depending on the chirality's handedness (see in Fig. 1.2). The fascinating phenomenon is noticeable in that a platform of the CISS is given by pure organic systems with light elements where a spin-orbit interaction (SOI) is negligibly small. Indeed, spin momentum locking can explain both large spin-orbit interaction and spin polarization; unexpectedly large spin polarization in CISS, especially at room temperature, could not be clearly introduced by spin momentum locking due to small SOI in organic molecules. Therefore, a great effort devoted from researchers

has been pursuing to hypothesize some mechanisms in CISS that how SOI effect enhances in organic molecules, which is the main heart of CISS effect. Thus far, although a microscopic origin of the unexpectedly large spin polarization of CISS has been still controversial,[14,15] the CISS effect potentially paves the way to a novel method of embedding organic chiral materials into solid-state spintronic and optical devices.[9,11,16]

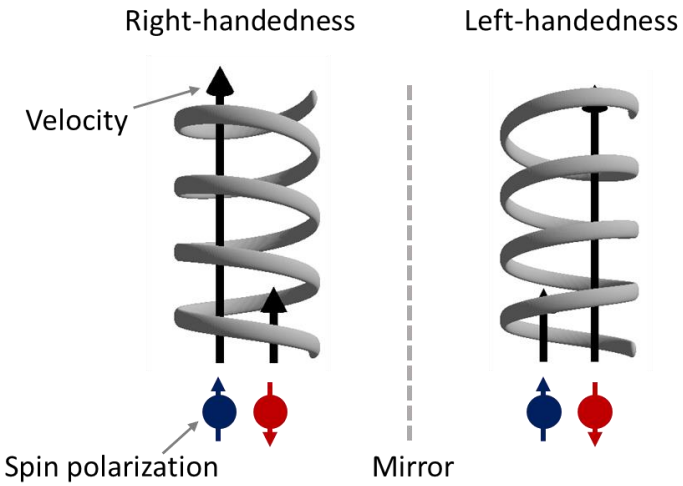

Fig. 1.2 Schematic of the CISS. Electrons get spin-polarized after transmitting through a chiral system. The spin-polarized direction depends on its chirality.

Since the discovery of CISS, significant studies have been intensively validated both theoretically and experimentally. Particularly, CISS has been experimentally verified in many kinds of experiment such as photoelectron spectroscopy,[17,18] magnetoresistance (MR) measurements,[19–21] magnetic conductive atomic force microscopy (mC-AFM),[19,22–24] and Hall voltage detection.[25,26] The CISS was also observed in various organic molecules such as DNAs,[27,28] oligopeptide,[29–31] helicene,[24] and supramolecular polymer.[32] Therefore,

considerable research interest in CISS effect has been focusing on fundamental studies to indeed understand the mechanism of CISS by developing and utilizing new materials and novel methods for further potential applications. This introduction part, providing will present and discuss an overview of CISS theory as well as the status of CISS experiments, and several applications of CISS that have been reported throughout the years.

1.2 The theoretical aspect of CISS

To explain CISS theory, in which spin selectivity is desired from the chiral molecules, a simplified model of molecular helicity has been proposed. Electron propagation through chiral molecules with electrostatic potential, a magnetic field is generated by current in chiral molecule. The dependence of magnetic field strength is due to the spin-orbit interaction (SOI), the interaction of the electron momentum and its spin. Because electron in chiral molecule has a magnetic dipole that is associated with its spin, two spin states generated when no magnetic field exists are now split. Therefore, SOI due to the situation, can be written using Hamiltonian as equation 1.1.[12,13]

$$H_{SOI} = \lambda\vec{\sigma} \cdot (\vec{p}\ x\ \vec{E}chiral) \qquad \textbf{Equation 1.1}$$

Where $\lambda = (e\hbar)/(4m^2c^2)$, $\vec{p}$ = the electron momentum, m = the electron's mass, and $\vec{\sigma}$ = a vector whose components are the Pauli matrices (σ_x, σ_y, σ_z). The interaction of momentum and its spin plays a crucial role in charge propagation through a helical molecule. To explain this, the propagation of an electron spins has four states written by I+,+>, I-,->, I+,->, I-,+>, where the first variable is the electron velocity direction and the second is the spin direction (see in Fig. 1.3). For left-handedness, an electron moves through molecule in positive direction, with its up spin (+) more stable than its down spin (-). A gap is twice as large as H_{SO}, where H_{SO} is the spin-orbit

energy. Conversely, an electron moves through chiral molecule in a negative direction, its spin down (-) is more stable than its spin up (+) with $2H_{SO}$. In the case of right-handedness, the situation becomes the opposite. Eventually, a spin polarization can be generated.

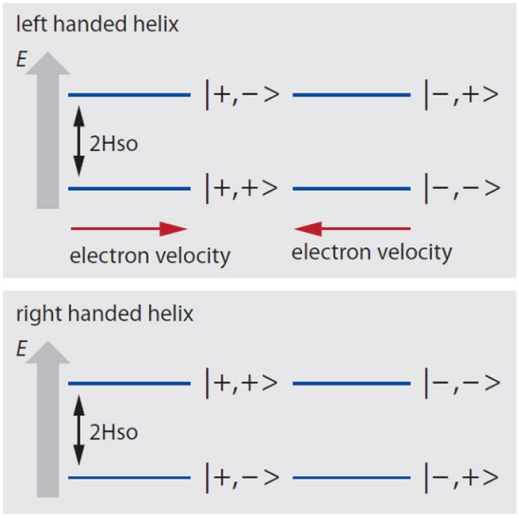

Fig. 1.3 Schematic for the electron spin states, |velocity, spin⟩, of an electron transporting in chiral helicity with electrostatic potential.[12]

As mentioned above, the spin polarization efficiency depends on the magnetic field strength, generated by the electron propagation through either the chiral electric field or, more specifically, on the strength of the SOI. The magnetic field strength inside the helicity can be approximately calculated with force, which must be large enough to keep the electron inside the helicity. The effective magnetic field can be written as equation 1.2.[10]

$$\left|B_{eff}\right| = \frac{mV}{qr} \qquad \textbf{Equation 1.2}$$

Where m is the mass, v is the electron velocity, q is the electron's charge, and r is the helicity's radius. This equation can be reformulated using H_{SOI}.

$$H_{SOI} = \frac{g}{2}\mu_B \left|B_{eff}\right| = \frac{g\mu_B mv}{2qr}$$ **Equation 1.3**

Where g is the g-factor of the electron, and μ_B is the Bohr magneton. Consider an electron with kinetic energy 1 eV ($v = 6x10^5$ m s^{-1}) and a radius of helicity is 0.5 nm. The H_{SOI} will be 360 meV. Therefore, the energy splitting between the states, which is $2H_{SO}$, is large enough to explain the CISS effect. However, it is believed that an electron cannot feel the magnetic field produced by its own motion.

After this prototypical theory, a great number of theoretical studies have been qualitatively proposed in the explanation of the experimental spin polarization, which suggests a highly significant interaction between electronic spin and electron motion in chiral structures. Thus, spin-orbit interaction (SOI) could play an essential role in the emergence of the CISS. However, a concrete theoretical model is still lacking to explain the CISS "qualitatively" because the SOI strength of an organic molecule is typically small. Later works have considered various factors to enhance the SOI, such as electron-electron correlation[33], exchange interaction[34], molecular vibration[35], friction dissipation[36], and Berry force[37]. However, no consensus has been reached so far.

1.3 Experimental CISS studies

Having provided the theoretical presentation above, next, several literature reviews will be presented and discussed about experimental studies to overview the interaction between electron spin and electron motion in chiral system. In the experimental section, CISS phenomena observed since the first discovery, can be widely distinguished in three main parts: CISS in electron transmission, CISS in electron transport, and CISS in chemical reactions.

1.3.1 CISS in electron transmission

The first finding of CISS in electron transmission was experimentally observed by the Ray group. They studied how the photoelectrons, in which electrons with circularly polarized light (CPL) excitation emit from gold substrate, transmitted through chiral molecular layer which is formed by the L- or D-stearoyl lysine (chiral amino acid) embedded on gold substrate.[38] They clearly found that the number of photoelectrons with clockwise (CW) light excitation corresponding to right-handed CPL (RCPL) is dramatically more prominent than that of counter-clockwise (CCW) light excitation corresponding to left-handed CPL (LCPL) for L-stearoyl lysine film. In contrast, the number of photoelectrons with RCPL excitation is smaller than that of LCPL excitation for D-stearoyl lysine film (see in Fig. 1.4). This phenomenon implies that the different handedness influences the number of selective-photoelectrons with circularly polarized light excitation. Later work was demonstrated by Carmeli et al.,[39] who studied the transmission that is similar to the previous experiment by using a polyalanine as chiral molecule (L- or D-form corresponding to left- or right-handed chirality, respectively) in the form of self-assembled monolayer on gold substrate. As illustrated in Fig. 1.5a, the photoelectrons, excited by both RCPL/LCPL to generate spin polarization (up or down), traveled through chiral molecule to exhibit asymmetries in the number of photoelectrons. Remarkably, Carmeli's work also implied that the spin polarization direction depends on the handedness and the molecular dipole direction. The dipole direction was inverted by changing the termination position of polyalanine to the gold substrate from the terminated-carboxyl group side to the terminated-amine group side, resulting in the sign inversion of the signal (asymmetry in the number of photoelectrons under RCPL excitation as compared to that under LCPL excitation).

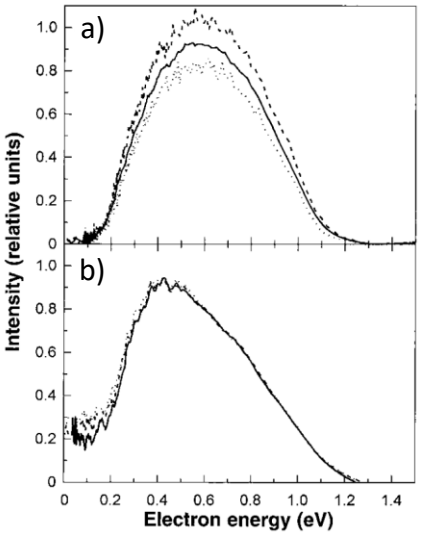

Fig. 1.4 Electron energy distribution of a) L-stearoyl lysine b) 99% L-stearoyl lysine and b) 1% D-stearoyl lysine. The photoelectrons were ejected with linearly polarized light (solid line), RCPL (dashed lines), and LCPL (dotted lines).[38]

The CISS was later verified by the Göhler and coworkders, who performed photoemission with Mott polarimeter to directly measure the spin polarization direction (up or down) of photoelectrons from gold thin film embedding a monolayer of double-stranded DNA (dsDNA).[9] A significant spin polarization was not only observed from CW/CCW light excitation, but also were observed from linearly polarized light excitation (see in Fig. 1.5b). Interestingly, they also found that spin polarization is enhanced by increasing the length of the dsDNA. The spin polarization for dsDNA containing 78 base pairs exceeded 60% at room temperature. In further verification of CISS in electron transmission, M. Kettner et al. confirmed the demonstration of the spin polarization direction depending on the chirality of the heptahelicene.[40] This implied that the chirality induces spin selectivity in the transmission, that is CISS being observed

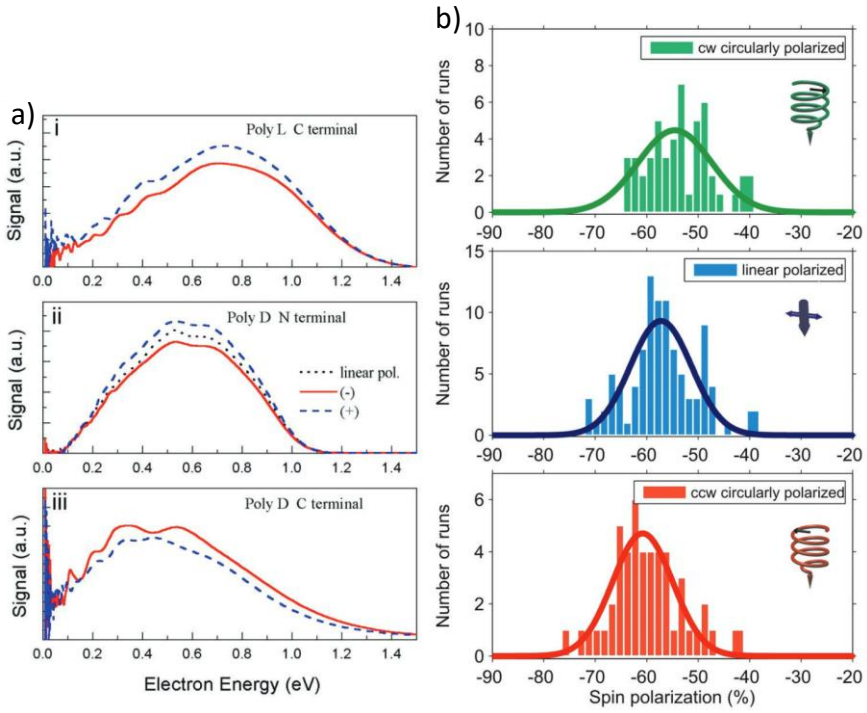

Fig. 1.5 a) Electron energy distribution for (i) C-terminal (L), (ii) N-terminal (D), and (iii) C-terminal (L). The photoelectrons were excited using a RCPL (red, solid), LCPL (blue, dashed), or linearly (black, dotted) polarized light. b) Spin polarization, measured for electrons ejected from an Au-coated substrate with a monolayer of 78 bp dsDNA.[9,39]

1.3.2 CISS in electron transport

The CISS in electron transport has been first verified by Z. Xie et al. They studied conductance through double-stranded DNA (dsDNA) oligomer using spin-polarized current. The oligomer acted as spin filter in the conductive atomic force microscopy (AFM).[41] As depicted in Fig. 1.6a, the AFM measurements were performed under magnetic field which was produced by the magnet with up or down magnetization pointing toward the nickel (Ni) ferromagnetic substrate. The current was flowing between two electrodes; Ni substrate through chiral molecule to gold

nanoparticles and then to the platinum electrode coated tip of the AFM. As a result, the *I-V* curves were recorded, as shown in Fig. 1.6b. They found that the conductance of the Ni-dsDNA-Au junction depends on the magnetization direction. In contrast, the magnetization dependence disappeared in a symmetric junction of Au-dsDNA-Au. This result indicates that the magnetization direction of Ni electrode affects the conductance of dsDNA junction. CISS in electron transport is detected not only in a conductive AFM but also in as magnetoresistance in a thin film device where one electrode is ferromagnetic, and the other is paramagnetic.[42,43] Electrochemical measurements with a ferromagnetic electrode were also verified.[44]

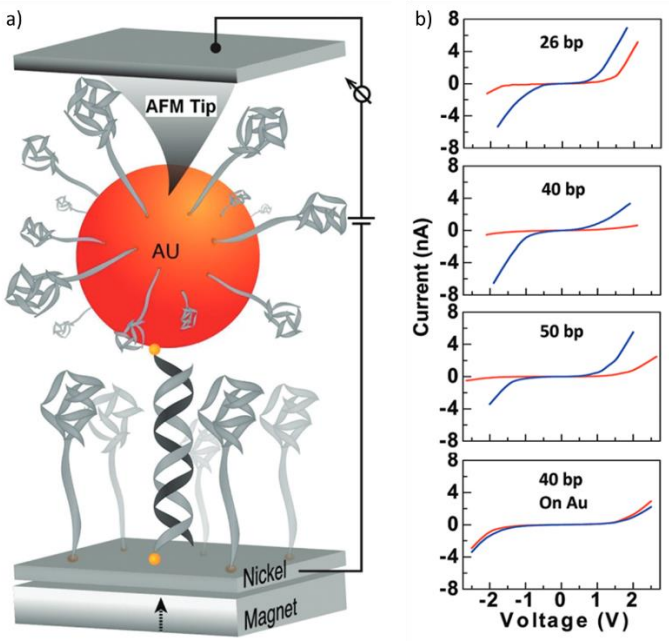

Fig. 1.6 a) Schematic of measurement set up and b) Nonlinear I-V curves of three oligomers with up (red) or down (blue) magnetization.[41]

S. P. Mathew et al. fabricated a magnetoresistance (MR) device, one of extensive methods to obtain CISS in electron transport where a chiral self-assembled monolayer of cysteine or polyalanine was sandwiched with ferromagnetic and nonmagnetic electrode.[45] As illustrated in Fig. 1.7, MR-based SAM devices comprising of L or D cysteine were measured and examined. Two devices exhibited significant opposite signal profiles of asymmetric magnetization curves as the function of the magnetic field. The difference is due to the different chirality handedness, with which electron's favored-spins become opposite. Besides, MR efficiency observed from the experiment was up to 20% at room temperature. The devices presented here operate with spins perpendicular to the substrate, therefore, can be an important building block for magnetic memory.

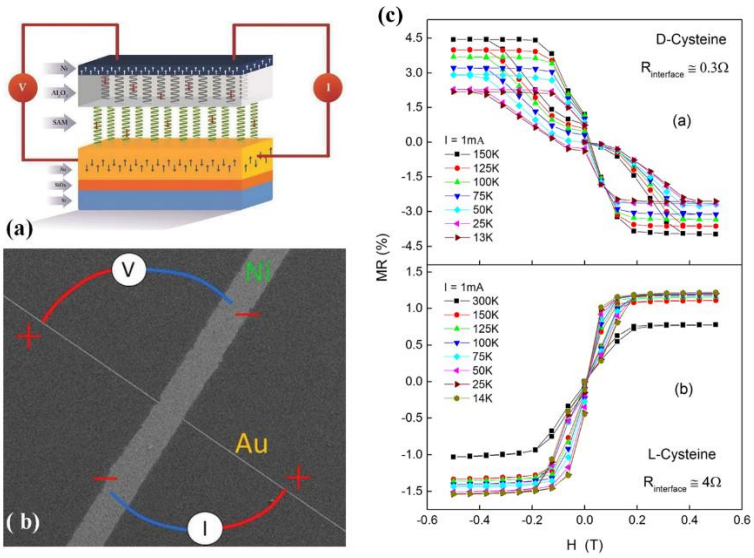

Fig. 1.7 (a) Scheme of four-terminal device (Au/SAM/Al_2O_3/Ni) for MR measurement and (b) Top view of SEM topography. (c) magnetoresistance of D-cysteine and L-cysteine.[45]

Moreover, for CISS verification in electron transport, especially in single device, M. Suda *et al*. utilized a molecular motor of overcrowded alkene (OCA).[46] The molecular motor with unidirectional 360º rotation around carbon-carbon double bond can be switched in four different steps: two light irradiation and two thermal treatment steps. Also, chirality, namely P (right-handed) or M (left-handed) forms switched by external excitation can invert the spin polarization direction of the electrons that pass through the molecular motors.[47,48] As can be seen from Fig. 1.8, the chirality of OCA can be switched by light shining or heat process, which allows them to control the spin selectivity direction by external stimuli. The CISS molecular switch-based devices, capable of switching the spin polarization direction, were performed by magnetoresistance (MR) and magneto-conductive atomic force microscopy (mC-AFM) measurements. As a result, they successfully demonstrated the chirality dependence of spin polarization direction by changing the chirality in a single device, which can eliminate experimental error such as device dependence. Thus, this result can be understood as solid evidence for the chiral-induced spin selectivity in electron transport.

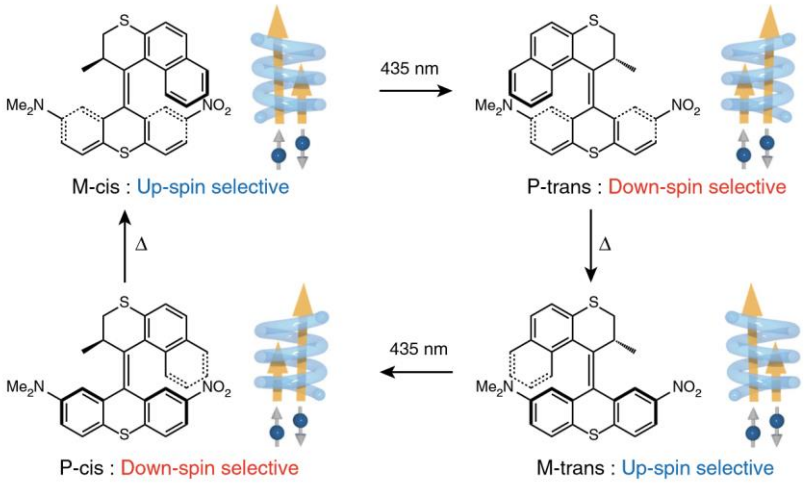

Fig. 1.8 Molecular structures of OCA with 360º unidirectional rotation switched by light/heat process as well as inverted spin polarization direction.[46]

1.3.3 CISS in chemical reaction

CISS in electron transmission and electron transport has been repeatedly observed; researchers, however, also use electron spin as an enantio-selective chemical reagent, which is the new opening of CISS application.[49,50] The original idea was traced back to Rosenberg et al. work, and it demonstrated that spin polarization at low energy, which were produced by irradiating a ferromagnetic substrate, results in different bond cleavage rates for R and S enantiomers of a chiral molecule adsorbed on the substrate.[51] In later work, K. Banerjee-Ghost et al. suggested that in chiral molecule, charge redistribution process manifests an enantiospecific preference in spin polarization when the molecules approach magnetic substrate.[52] This work was anticipated that the exchange interaction between the enantiospecific spin orientation and perpendicularly magnetized substrate could possibly interact, which allows one to separate a racemic mixture into its two enantiomers by simply exposing the mixture to the magnetic substrate. They experimentally demonstrated an enantiospecific interaction between a chiral molecule and a magnetized surface, in which chiral molecules (L- and D-polyalanine) were exposed to surface substrate with perpendicularly magnetized ferromagnetic cobalt film covered with gold for 2 sec. As a result, L-PAL is preferentially adsorbed on the substrate when magnetic dipole is pointing up. On the one hand, D-PAL is preferentially adsorbed on the substrate when magnetic dipole is pointing down (see in Fig. 1.9A). Additionally, after a racemic mixture was exposed to the surface for 2 sec, they subsequently measured circularly dichroism (CD) experiments for the residual solution. As shown from Fig. 1.9B, the signal profiles for D- and L-PAL are remarkably different after exposing the mixture to up- or down-magnetized substrate, respectively. This signature corresponded to the situation where one of the enantiomers was selectively adsorbed on the film magnetized with a specific direction, resulting in an enantiomeric excess in the residual solution. Their experiments

clearly showed enantiomeric separation based on the CISS effect. Note that the enantiomeric separation could not be obtained when the mixture was exposed to the ferromagnetic film for a long time (2 min). However, the separation occurred only in a short time experiment (order of seconds). It means the enantiospecific interaction is kinetic, not thermodynamic, which gives one a clue to the origin of the enantiospecific interaction with the ferromagnet.

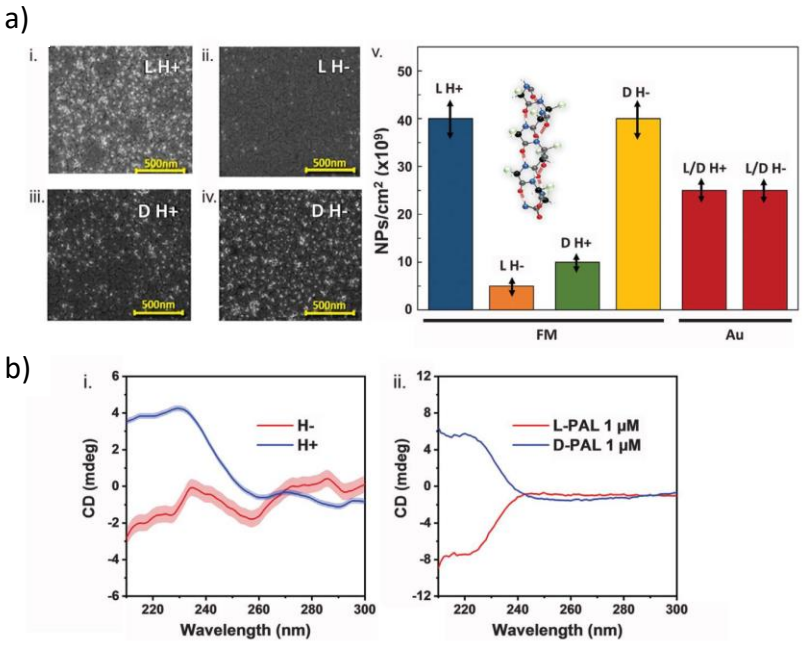

Fig. 1.9 a) SEM images for adsorption of the PAL oligopeptide adsorbed onto the ferromagnetic substrate with up magnetization (H^+) or down magnetization (H^-) [(i) and (ii) L-PAL, (iii) and (iv) D-PAL, and (v) summarizes the density of nanoparticle adsorption shown in (i) to (iv), compared with the adsorption density onto the paramagnetic substrate as Au under magnetization (red bars). b) CD spectra of PAL under magnetization, (i) racemic mixture and (ii) pure enantiomers.[52]

As can be seen from Fig. 1.10, They also explained how enantiospecific spin polarization rationalized in terms of CISS in the chiral molecule, which reveals the selective magnetic exchange interaction with the ferromagnetic substrate, in which spin orientation appeared in the form of the accumulation of an antiparallel spin pair at the two opposite terminals of a chiral molecule. Suppose an exchange interaction occurs between the accumulated spin at the terminals of the chiral molecule and the spin at the ferromagnetic substrate. In that case, the interaction of substrate-molecule should be stabilized when two spins are antiparallel, whereas the substrate-molecule interaction should be destabilized when two spins are parallel. This situation leads to the selective adsorption of the chiral molecule on the perpendicularly magnetized ferromagnet.

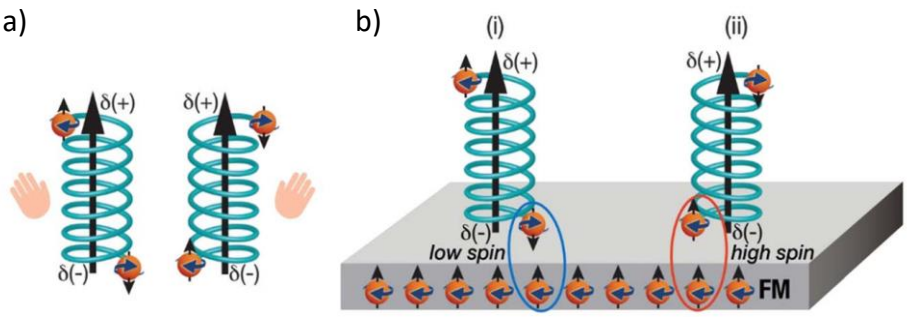

Fig. 1.10 a) A schematic of spin polarization, in which spin orientation at each electric pole depends on the handedness molecule. b) The interaction between the ferromagnetic substrate and the molecule, in which a low-spin (i) or a high-spin (ii) potential depends on the magnetization direction of the substrate.[52]

In summary, in this introduction part, both theoretical and experimental reports on CISS have been presented. Remarkably, three surveys (CISS in electron transmission, electron transport, chemical reaction) demonstrated that CISS has a crucial fundamental effect, with many

manifestations and practical consequences in several areas, from spintronics to chemical reactions. Therefore, this part extremely interests me and brings me to intensively study to pave the way for understanding and utilizing CISS in further practical applications.

Chapter 2

Study of Materials for CISS

Since the discovery of CISS as mentioned previous chapter (CISS in electron transmission, CISS in electron transport, CISS in chemical reaction), a variety of chiral materials such as biomolecules, supramolecular polymers, metal-organic frameworks, inorganic bulk crystals, and chiral molecular intercalation superlattices has been extensively observed, which suggest that CISS is universal in the chiral system. However, most of them used in the experiments are fixed-handedness molecules; two different devices using molecules with opposite chirality are involuntarily prepared to discuss a coupling between CISS effect and molecular chirality, inevitably giving ambiguities in that many properties other than chirality change. Therefore, the manipulation of spin polarization (SP) direction by external stimuli has not been studied. Therefore, the development of switchable organic molecules in "single device", capable of inversion of the spin polarization is considerably desired to study. In this chapter, molecular switching based on external controllability will be studied and presented in detail.

2.1 Molecular motor based on overcrowded alkenes

Molecular motor, a class of molecular machine has played a crucial role as a source to generate unidirectional mechanical motion. Particularly, molecular motors based on overcrowded alkenes (OCAs) was first discovered in 1999 by Feringa et al., capable of performing repetitive unidirectional 360° rotation.[53,54] Overcrowded alkenes have a unique central double bond

connecting between the upper and lower parts. The first generation of molecular motor featured two stereogenic methyl substituents which determine the direction in a pseudoaxial orientation due to steric crowding. These stereocenters dictate the helical chirality in both parts of the molecule and influence the 360° rotation consisting of four steps: two-light irradiation process and two-heat treatment process.

As can be seen from Fig. 2.1a, starting from chirality of (*P*,*P*)-trans, irradiated by light with the wavelength >280 nm, (*P*,*P*)-trans results in inverting to (*M*,*M*)-cis with opposite chirality. This process is reversible, but (*M*,*M*)-cis can be observed under continuous irradiation (photostationary state). For (*M*,*M*)-cis at this state referred to as unstable state, the methyl substitution is unfavorable with pseudoequaterial structure. To release the stressed structure, thermal process can treat the helicity of (*M*,*M*)-cis by inverting to (*P*,*P*)-cis which allows the favorable pseudoaxial structure, resulting in 180° rotary motion. The second part of the cycle proceeds similarly to a second irradiation process that provides (*M*,*M*)-trans (the methyl substituents again in the pseudoequatorial position). A second thermal treatment then reforms (*P*,*P*)-trans, and a full 360° rotation cycle is completed. A molecular motor based on overcrowded alkene has four rotational steps via carbon-carbon double bond and each step has energy profile as shown in Fig. 2.1. Fig. 2.1b depicts the mechanism of each rotational step which is a fascinating in chiral switching with stereogenic center, in which the chirality switches in every rotational step by external stimuli and stereogenic methyl-substitution also dictates the rotation direction. In photoirradiation process with uphill isomerization, the system is in equilibrium with unstable form, but at the same time, thermal treatment with downhill isomerization returns the OCA to the stable form. With this system, the OCA would be able to switch the chirality by photoirradiation and heat treatment, contributing to repeatable process.

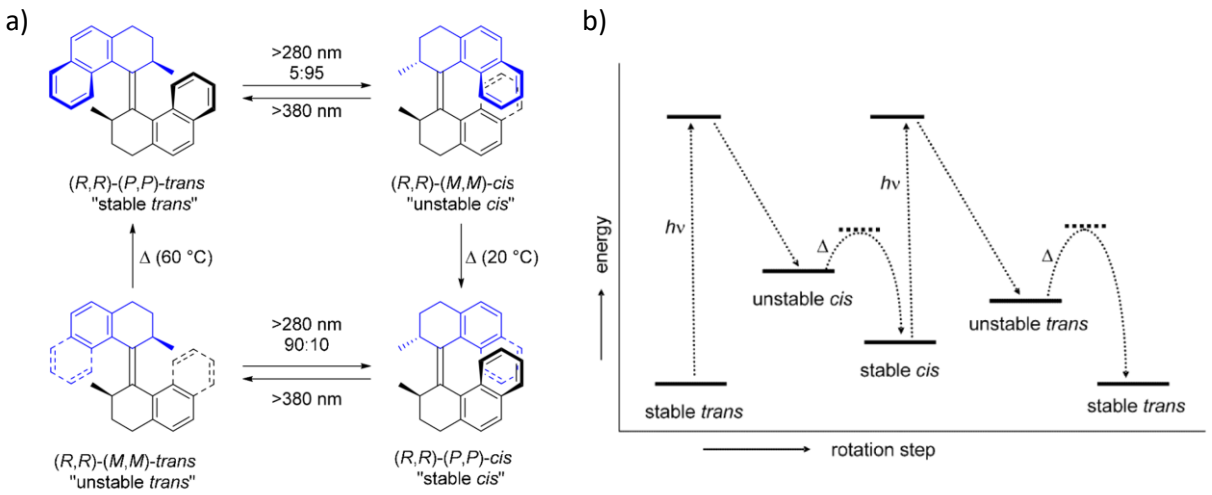

Fig 2.1 a) mechanism for unidirectional 360° rotation for the first generation of OCA. b) general energy profile for the 360° unidirectional rotation.[54]

However, a drawback for the first generation of OCA is the difference in the activation barrier for the heat treatment steps. A haft of the 360° rotation is considerably faster than the other, resulting in an irregular rotation. The second generation of OCA can address this issue,[55,56] in which the lower part is a symmetry which is usually fixed and acted as stator to provide the motor, and the upper part is an asymmetry acted as rotor (see in Fig. 2.2). The second generation of OCA was modified to provide similar activation barriers which contributes to more uniform rotation. Notably, even though the second generation of OCAs was structurally modified from the first generation, but the mechanism of rotational step is still the same to account for its functioning as a unidirectional molecular motor based on OCA.

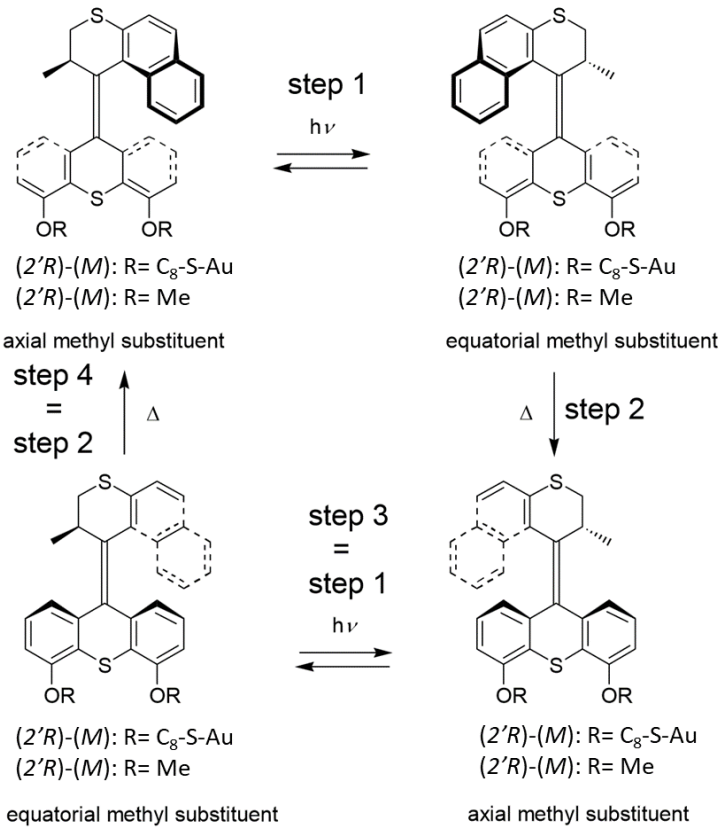

Fig 2.2 Mechanism for unidirectional 360° rotation for the second generation of OCAs.[56]

In addition, a significant advantage of second-generation motors is that they can functionalize either upper (rotor) or lower (stator) parts, for instance, in surface embedding which would expand research in extensive applications. Particularly, the symmetric lower part of the second-generation molecular motors (Fig. 2.3) can be used for functionalization of the ultimate connection of the molecular motor to a surface. In contrast, the upper part still acts as a rotator. For example, attaching the molecular motor based on OCA appropriately to a solid support transforms the relative rotary motion of the upper part with respect to the lower part into absolute rotary motion relative to the support. It is crucial that the OCA with two thiol-terminated alkyl chains as legs is embedded to the gold (Au) surface through two alkyl chain-functionalized thiols.

The chains should be long enough to provide the space for rotating molecules as well as avoiding interference or quenching by gold surface. In this case, an eight-carbon chain was chosen,[57] which could influence a 360° unidirectional rotation by photoirradiation and heat treatment process.

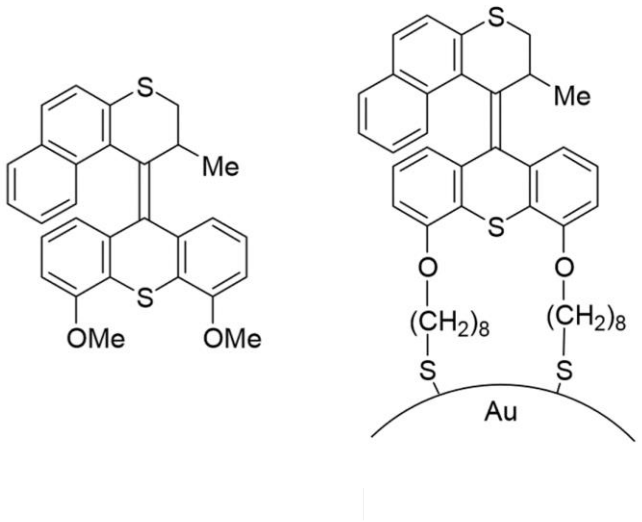

Fig. 2.3 The dimethoxy substituted OCA and OCA-alkanethiol functionalized gold.[56]

2.2 Triglycine sulfate (TGS)

Thus far, most CISS studies have intensively focused on chiral metals or insulating organic monomolecular layers to experimentally discuss spin-polarized current. Then a fundamental question arises on CISS effect in chiral ferroelectric materials because charge transport in macroscopic ferroelectric materials is only possible with displacement current. Therefore, an emergent spin-polarized current, if any, is a new category of CISS using the displacement current. Ferroelectric chiral materials have attracted much interest due to unique ability with which both the polarity and chirality can be inverted in ferroelectric phase under electric filed.[58] Polarity-

and-chirality relationship, referred to as absolute polarity, of a ferroelectric material, is of profound significance in solid-state device.[59]

Triglycine sulfate $(NH_2CH_2COOH)_3 \cdot H_2SO_4$ (TGS), which is a transparent ferroelectric material, was first studied and investigated by Hoshino team. TGS can form chiral crystals with a ferroelectric phase transition of order-disorder type at a transition temperature or a Curie temperature (T_C) of 322 K.[60] In TGS crystal as achiral is at the paraelectric phase above T_c with the space group and point group of $P2_1/m$ and C_{2h}, respectively. TGS crystal becomes chiral at ferroelectric phase below T_c with the space group and point group of $P2_1$ and C_2, respectively.[61,62] Fig. 2.4 shows the TGS crystal, in which spontaneous polarization (Ps) direction is along to the b-axis below T_C; the b-axis dielectric constant also manifests a sharp but continuous peak at T_C.[63,64]

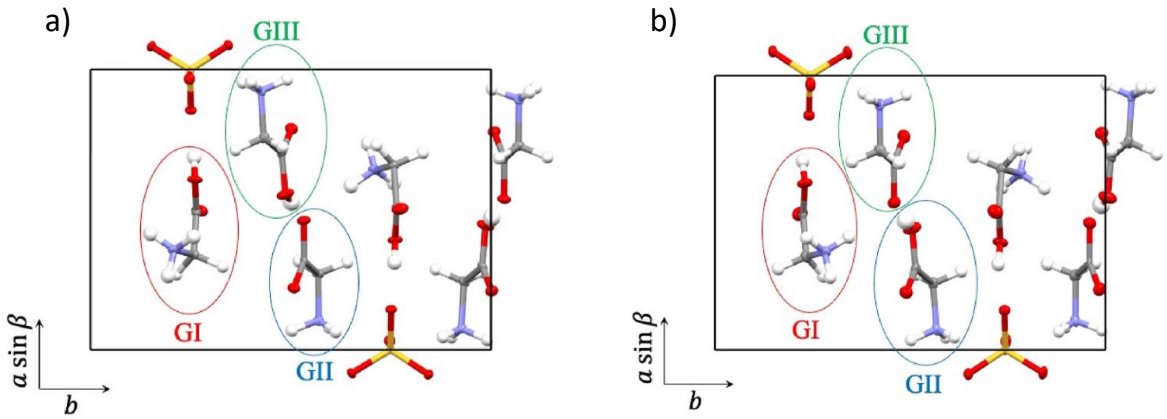

Fig. 2.4 TGS crystal structure in the unit cell a) negative polarity and b) positive polarity. Yellow, red, purple, grey, and white balls represent sulfur, oxygen, nitrogen, carbon, and hydrogen, respectively. Glycines shown as open red, blue, and green circles are Glycine I (GI), Glycine II (GII), and Glycine III (GIII), respectively.[65]

Having introduced a unique handedness, which are imposed throughout the entire crystal by poling process with decreasing temperature from the achiral phase at high temperature under electric field along to *b*-axis, chirality with its opposite handedness (positive and negative polarity) that become chiral phase below T_c can be distinguished and characterized by single crystal analysis using X-ray diffraction analysis. By reversing polarization, the structural change has been made by the motion of the hydrogen atoms between oxygen atoms, rotation of the glycine I group, and by changing of the hydrogen bonds connected to nitrogen atoms of the glycines II and III (see in Fig. 2.5).[65–67]

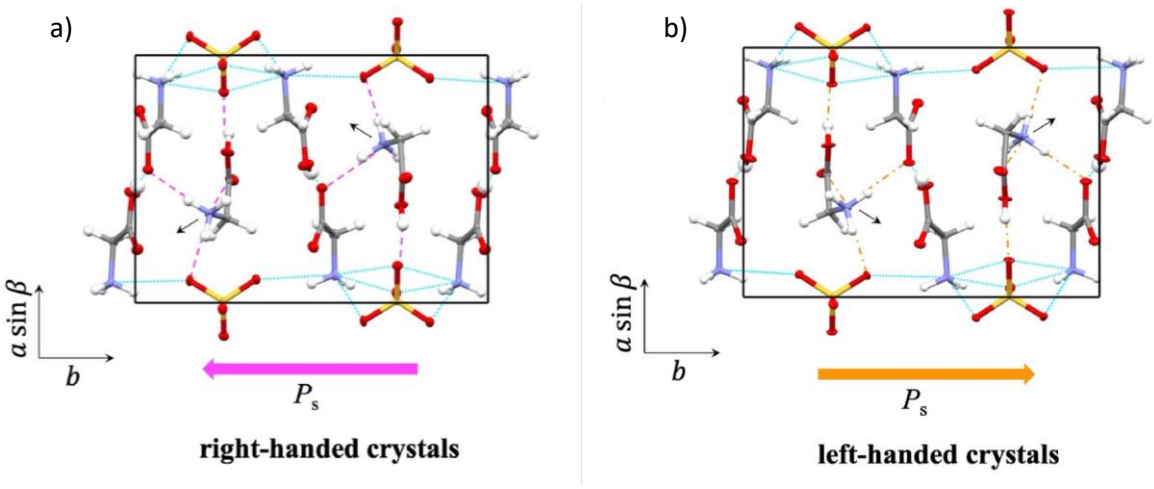

Fig. 2.5 The crystal structure of TGS. The atomic arrangement of (a) negative polarity and (b) positive polarity.[65]

As mentioned above, molecular motor based on overcrowded alkene (OCA) and ferroelectric material based on triglycine sulfate (TGS) exhibit the ability to control chirality. Both OCA and TGS will be experimentally studied and discussed to verify CISS in chapter 3 and chapter 4, respectively.

2.3 Purpose of thesis

To date most studies on the CISS effect have used fixed handedness of chiral molecules, namely, molecules whose chirality is inherent to them and thus cannot be changed. In these experiments, the results are inevitably giving ambiguities in that many other properties other than chirality also change. In this point of view, a single device in which the chirality can be externally switched is highly desired. Two different CISS devices using molecules with opposite chirality are involuntarily prepared to discuss the coupling between CISS effect and molecular chirality.

Considerable interest in CISS lies in switchable chiral molecules with external controllability as first presented in chapter 3 **"(i) Highly Durable Spin Filter Switching Based on Self-Assembled Chiral Molecular Motor"**. By studying molecular motors based on overcrowded alkenes (OCAs), their handedness are switched by light irradiation and heat treatments. In a previous study, OCA-based devices that exhibit CISS remains far from completion in terms of practical use, and rather fundamental obstacles such as (i) external controllability of spin, (ii) function durability, and (iii) improvement of spin-polarization efficiency have yet to be surmounted. Therefore, I aim to prepare new molecular systems based on overcrowded alkene that can address the three obstacles mentioned above to develop the practical utilization of CISS effect.

In the second work, my significant research interest focuses on ferroelectric chiral materials as triglycine sulfate (TGS), which will be presented in chapter 4 **"(ii) Engineering Surface Spin Based on Chiral dielectric Materials''** Thus far, most CISS studies have intensively focused on chiral metals or insulating organic monomolecular layers to experimentally discuss spin-polarized current. Then a fundamental question arises on CISS effect in chiral ferroelectric materials because

charge transport in macroscopic ferroelectric materials is only possible with displacement current. Therefore, an emergent spin polarization due to the displacement current, if any, is expected.

This thesis reports studies on **i) Highly Durable Spin Filter Switching Based on Self-Assembled Chiral Molecular Motor** and **ii) Engineering Surface Spin Based on Chiral dielectric Materials**. Both of the topics, where organic materials-based devices with chirality-control by external stimuli are employed, aim to experimentally study and to verify CISS effect. It is anticipated these works will be crucial in understanding and in utilizing CISS in further practical applications.

Chapter 3

Highly Durable Spin Filter Switching

Based on Self-Assembled Chiral Molecular Motor

Authors contributing to this study: Ruttapol Malatong, Takuro Sato, Jakkapan Kumsampao, Taketoshi Minato, Masayuki Suda, Vinich Promarak, Hiroshi M. Yamamoto

3.1 Abstract

Chiral molecules have recently remarkably received renewed interest as highly efficient sources of spin-selective charge emission known as chiral-induced spin selectivity (CISS), which potentially offers a fascinating utilization of organic chiral materials in novel solid-state spintronic devices. However, practical use of CISS remains far from completion, and rather fundamental obstacles such as (i) external controllability of spin, (ii) function durability, and (iii) improvement of spin-polarization efficiency have yet to be surmounted to date. In this study, I address these issues by developing a self-assembled monolayer (SAM) of overcrowded alkene (OCA)-based molecular motor. With this system, I successfully demonstrate that the direction of spin polarization can be externally and repeatedly manipulated in a highly stable manner by switching the molecular chirality, which is achieved by the formation of the covalent bonds between the molecules and electrode. In addition, I found that a higher stereo-ordering architecture of the SAM of OCAs tailored by mixing them with simple alkanethiols considerably enhances the efficiency of spin polarization per a single OCA molecule. All these findings provide a creditable feasibility

study for powerfully boosting the development of CISS-based spintronic devices that can simultaneously fulfill controllability, durability, and high spin-polarization efficiency.

3.2 Introduction

A gigantic spin-polarized current has recently emerged in organic chiral molecules, which is often referred to as chiral-induced spin selectivity (CISS). The phenomenon is noticeable in that a platform of the CISS is given by pure organic systems. To date, the CISS effect has been verified by numerous experiments as well as in a wide range of organic molecules. However, towards practical application of CISS, several fundamental obstacles such as improvements of (i) controllability, (ii) durability, and (iii) efficiency of the spin polarization remain to be accomplished, all of which are significant barriers to boosting a further development of the CISS-based molecular spintronic devices. Owing to the chiral-symmetrical constraint, the direction of spin polarization is determined solely by the handedness of the molecules. Therefore, static chiral molecules, in which the handedness are microscopically fixed by their chemical bonds, cannot invert the spin polarization direction[68–72], precluding the realization of externally controllable spin-switching devices.

These issues were prior addressed by using an overcrowded alkene (OCA)-based molecular motor where the chirality can be repeatedly switched by light irradiation and heat treatment[73–75] (Fig. 3.1). Consequently, a one-time reversal of the chirality (handedness) and the concomitant spin-polarization switching was observed in the solid-state device. Nevertheless, the function of producing spin-polarized current gradually deteriorates after several chiral switching processes.[73] The poor durability is attributable to an absence of chemical and/or physical stability of OCAs on

the substrate because of the simple fabrication method utilizing spin coating or drop-casting of the molecules without chemical bonding. In this case, the chiral-switching motion of the OCAs would induce a random rearrangement of the helical axis of each molecule or weaken molecular adhesion to the electrodes, possibly obscuring the experimentally detected spin polarization. Another fundamental issue in advance for the device application is to offer a simple method for improving the spin polarization efficiency of a chiral molecule. With these regards, the preparation of new molecular systems combining (i) controllability, (ii) durability, and (iii) improved spin polarization efficiency is increasingly demanded for further developing the practical utilization of CISS effect.

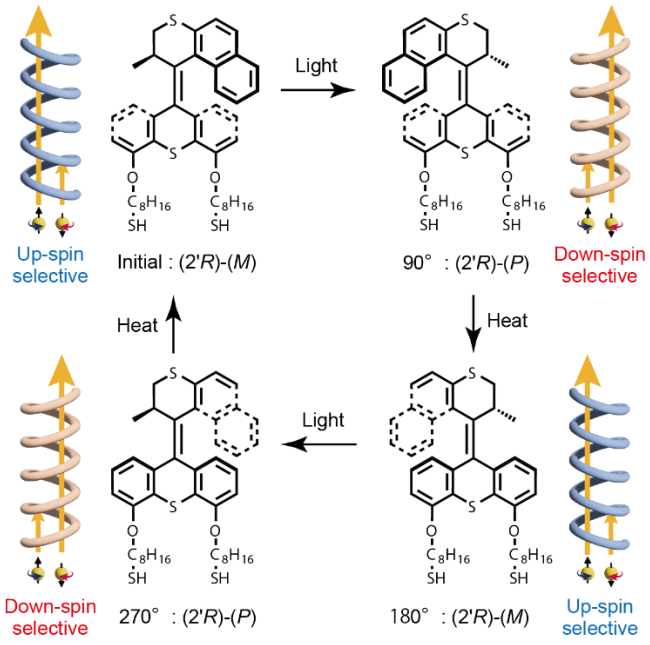

Fig. 3.1 Four-cycle 360° unidirectional rotations of the OCA molecule driven by light irradiation and heat application. (*2'R*)-(*M*)-OCA and (*2'R*)-(*P*)-OCA are characterized by the opposite handedness, and thus exhibit a spin selectivity with opposite directions.

With the above issues in mind in this study, I developed a self-assembled monolayer (SAM) of thiol-functionalized chiral OCAs on a ferromagnetic layer, in which the covalent bond between thiols and a metal electrode guarantees the stability of the spin-polarization functionality. In addition, by focusing on the stereo architecture of the SAM of the OCAs, I pursue a new route for enhancing the spin polarization efficiency per a single OCA molecule. The present feasibility study provides a solid foundation for the future practical application of CISS effect that can simultaneously overcome the three fundamental obstacles mentioned above.

3.3 Experimental

3.3.1 Synthesis and characterization of OCAs.

All reagents for the synthesis were commercially available and were used without further purification. The NMR spectra were recorded using 400 MHz nuclear magnetic resonance system (JEOL JNM-ECS400). The mass spectra were measured by a gas-chromatograph-connected mass spectrometer (GCMS-QP2010 SE). Circular dichroism (CD) spectra were measured by J-720WI (JASCO) in ethanol solution. The OCAs were successfully synthesized according to ref.[76,77] The synthesized two enantiomers of (2'*R*)-(*M*)-OCA and (2'*S*)-(*P*)-OCA were resolved by chiral HPLC through a CHIRAL ART Cellulose-SB (SMC) column using n-hexane: *i*-propanol (90:10). The elution times were 32 min and 40 min for (2'*R*)-(*M*)-OCA and (2'*S*)-(*P*)-OCA at flow rate of 4 mL/min., respectively. The enantiopurity in each state confirmed by HPLC was more than 95%.

3.3.2 Preparation of the substrates covered by Ni and Au

SiO_2 substrates were initially cleaned by acetone and isopropyl alcohol and treated with O_2 plasma (20 W/ 5 min). The substrates were then swiftly transferred to an electron-beam

evaporation system. I prepared thick ferromagnetic Ni capped by thin Au layers, whose thickness are 50 nm and 10 nm, respectively. Both Ni and Au were evaporated at rate of ~0.1 Å s^{-1} with a base pressure of approximately 10^{-5} Pa.

3.3.3 Fabrication of SAM of OCAs

Firstly, the metal-evaporated substates were washed by acetone 2-times followed by IPA. After the substrates were subsequently treated with O_2 plasma (20 W/5 min), they were immersed in absolute ethanol for 20 min and then finally placed into an ethanolic solution consisting of 1 mM OCA. I left them for a few days. After finishing the SAM adsorption, the substrates were immediately washed in absolute ethanol to remove the remaining residue and finally dried in Ar gas. After deposition of SAM is completed, the thiol terminals that are originally oxidized in air easily have already been inactive because of the formation of covalent bonds to Au surface, being robust to the air. Thus, I can safely conduct the mC-AFM measurements of the SAM in normal condition.

3.3.4 Magneto-conductive atomic force microscopy (mC-AFM).

mC-AFM measurements were performed by using the Dimension Icon XR (Bruker corporation). The Ni layer on the substrate worked as a bottom electrode, and was magnetized by permanent magnet, whose maximum field was around 260 mT, placed under the substrates. A motor connected to the magnet was able to rotate the orientation of magnet externally, making it possible to measure *I-V* profile of the SAM without moving the tip x-y location within the instrumental accuracy between up and down magnetized conditions. Actual measurement protocol is as follows; After measuring at least 50 *I-V* curves with applying positive magnetic field (the angle of the permanent magnet is 0°), I only slightly lifted up the tip by 40 nm from the substrate

surface, and then rotated the permanent magnet by 180° by PC to apply negative magnet field, immediately moving on the next measurements with negative field (see in Fig. 3.2).

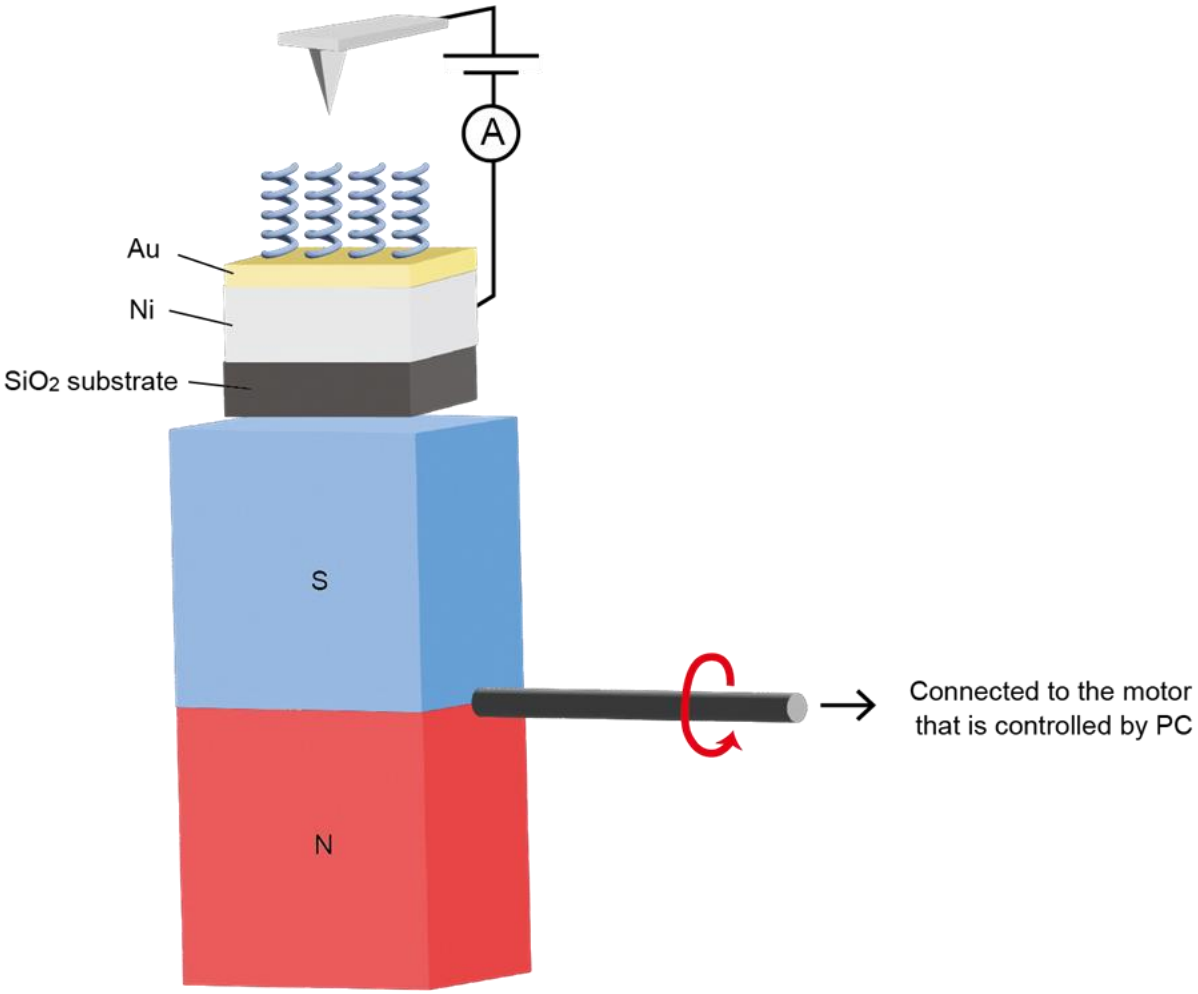

Fig. 3.2 Experimental configuration of mC-AFM. A permanent magnet is placed underneath the SiO_2 substrate. The angle of the magnet is able to being externally rotated by the PC-controlled motor.

Electric current was measured by contact mode with a diamond-coated Si tip (CDT-FMR-SPL, NanoWorld), whose spring constant is 6.2 N/m, with sweeping the biased voltage in the range of ±1 V. The applied force between the tip and the samples is kept at 180-190 nN not to give any damage to the molecules. At least 50 *I-V* curves were recorded and averaged for each chirality-rotation step and two magnetic orientations.

3.3.5 Irradiation and heat process

Visible light was irradiated from the topside of the substrates with a xenon light source (MAX-303: ASAHI SPECTRA). The wavelength of 465 ± 10 nm was selected using optical band-pass filters. The intensity of light is roughly 13 mW cm^{-2}. Heat treatment was employed using hot-plate at a temperature of 80 ºC.

3.4 Results and Discussion

3.4.1 Synthesis of thiol-functionalized OCA and fabrication of SAM of the OCAs.

The target molecule, overcrowded alkenes (OCAs) functionalized with thiol groups, was synthesized according to the reported procedure.[76,77] Fig. 3.3a illustrates schematics of the synthesis of OCAs. Asymmetric upper and symmetric lower parts were separately synthesized and were subsequently combined to form an intermediate compound bearing two methoxy substitution groups. In this structure, the lower and upper parts work as the stator and the rotor, respectively. The carbon-carbon double bond as the axle can induce a unidirectional twisting motion triggered by light irradiation and heat treatment, leading to chiral switching[76,77] (Fig. 3.1 and Fig. 3.3a). Finally, replacing the methoxy groups with alkyl chain (C_8) spacers terminated with thiols completed the fabrication of the target OCA (Fig. 3.3a). Note that the C8-spacers are necessary for

this study because they provide the free space to unidirectionally rotate the structure and interact with each other via an attractive van der Waals interaction that is essential for forming highly ordered assembly.[77] The molecular structure was confirmed by standard spectroscopic methods (GCMS and ^{1}H-NMR, ^{13}C-NMR, Fig. 3.4-3.7), all of which were in good agreement with the expected structures.[76,77]

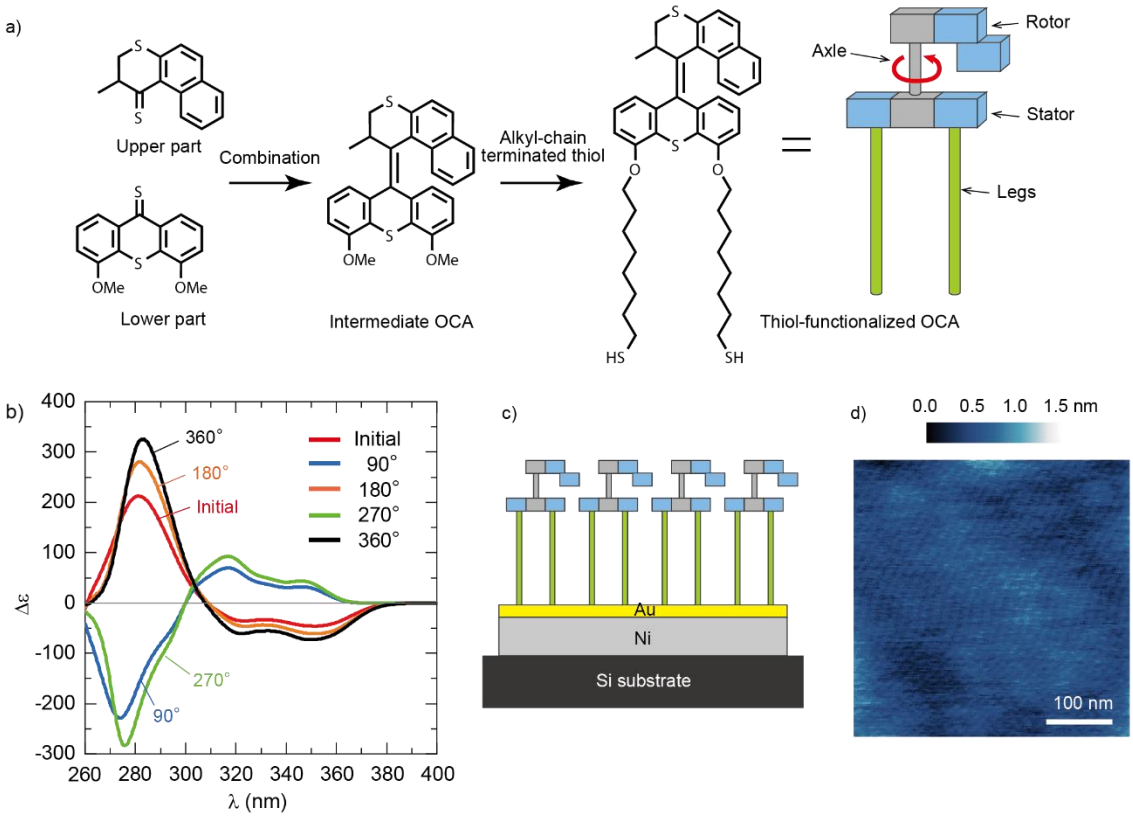

Fig. 3.3 a) A synthesis scheme of the thiol-functionalized OCA. b) CD spectra of the thiol-functionalized OCA in ethanol solution for each chiral-rotation step. c) Schematics of the self-assembled monolayer (SAM) of the thiol-functionalized OCAs formed on the Au/Ni-coated substrate. d) AFM topography of the prepared SAM of OCAs.

4,5-Dimethoxy-9-(2’,3’-dihydro-2’-methyl-1’H-naphtho[2,1-b]thiopyran-1’-ylidene)-9H-thioxanthene

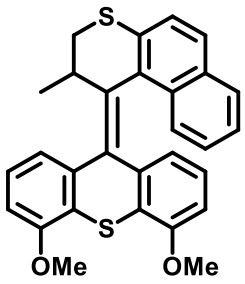

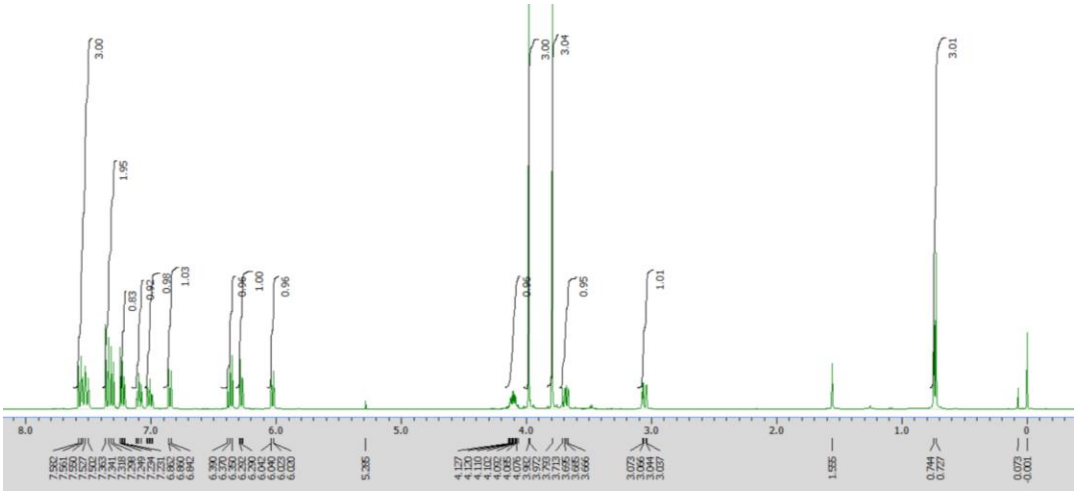

Fig. 3.4. ^{1}H NMR spectrum (400 MHz, $CDCl_3$) of the intermediate OCA.

The list of the chemical shifts in the unit of ppm is as follows; δ 0.73-0.74 (d, J = 6.8 Hz, 3H), 3.04-3.07 (dd, J = 11.6, 2.8 Hz, 1H), 3.67- 3.71 (dd, J = 11.2, 7.2 Hz, 1H), 3.79 (s, 3H), 3.98 (s, 3H), 4.07-4.14 (dqd, J = 7.2, 6.4, 2.8 Hz, 1H), 6.02-6.04 (dd, J = 7.6, 1.2 Hz, 1H), 6.27-6.29 (dd, J = 7.6, 1.6 Hz, 1H), 6.35-6.39 (t, J = 8.0 Hz, 1H), 6.84-6.86 (dd, J = 8.0, 0.8 Hz, 1H), 7.00-7.03 (m, 1H), 7.08-7.12 (m, 1H), 7.21-7.23 (dd, J = 8.0, 1.2 Hz, 1H), 7.30-7.36 (m, 2H), 7.50- 7.58 (m, 3H);

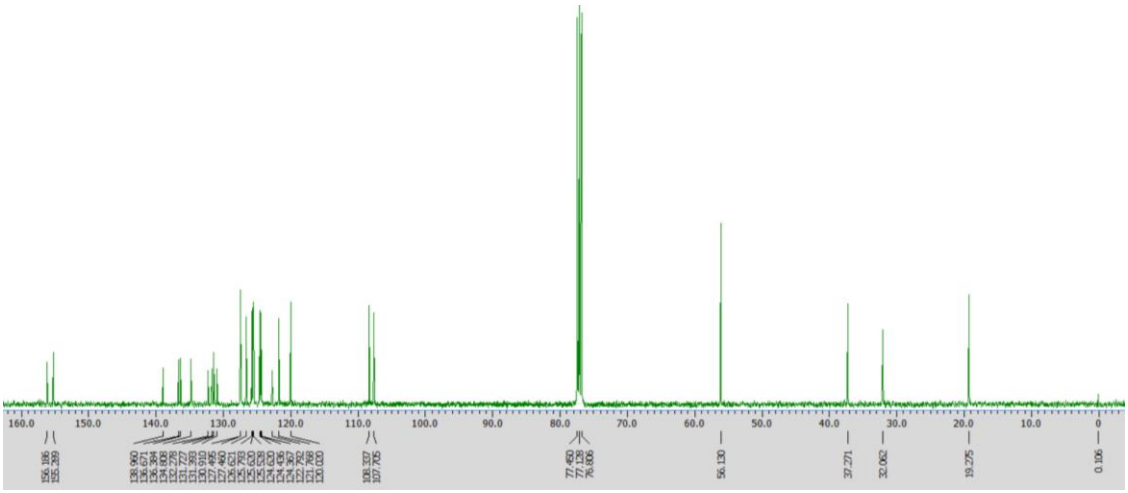

Fig. 3.5. ^{13}C NMR spectrum (101 MHz, $CDCl_3$) of the intermediate OCA.

The list of the chemical shifts in the unit of ppm is as follows; δ 19.3, 32.1, 37.3, 56.1, 107.7, 108.3, 120.0, 121.8, 122.8, 124.4, 124.4, 124.6, 125.5, 125.6, 125.8, 126.6, 127.5, 127.5, 130.9, 131.4, 131.7, 132.3, 134.8, 136.4, 136.7, 139.0, 155.3, 156.2

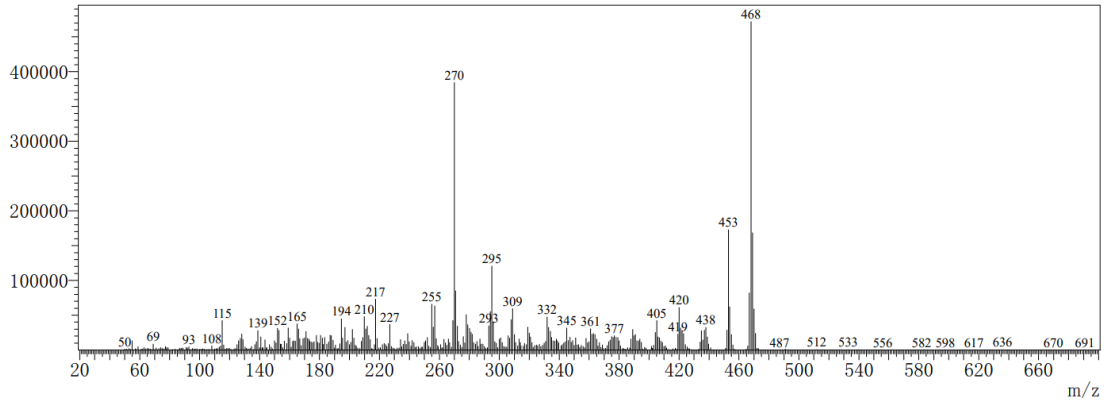

Fig. 3.6 GCMS spectrum of the intermediate OCA.

Experimentally evaluated *m*/*z* is 468 of the intermediate OCA, which is consitent with an expected value, 468.1218 from $C_{29}H_{24}O_2S_2$.

8,8'-((9-(2-methyl-2,3-dihydro-1H-benzo[f]thiochromen-1-ylidene)-9H-thioxanthene-4,5-diyl)bis(oxy))bis(octane-1-thiol)

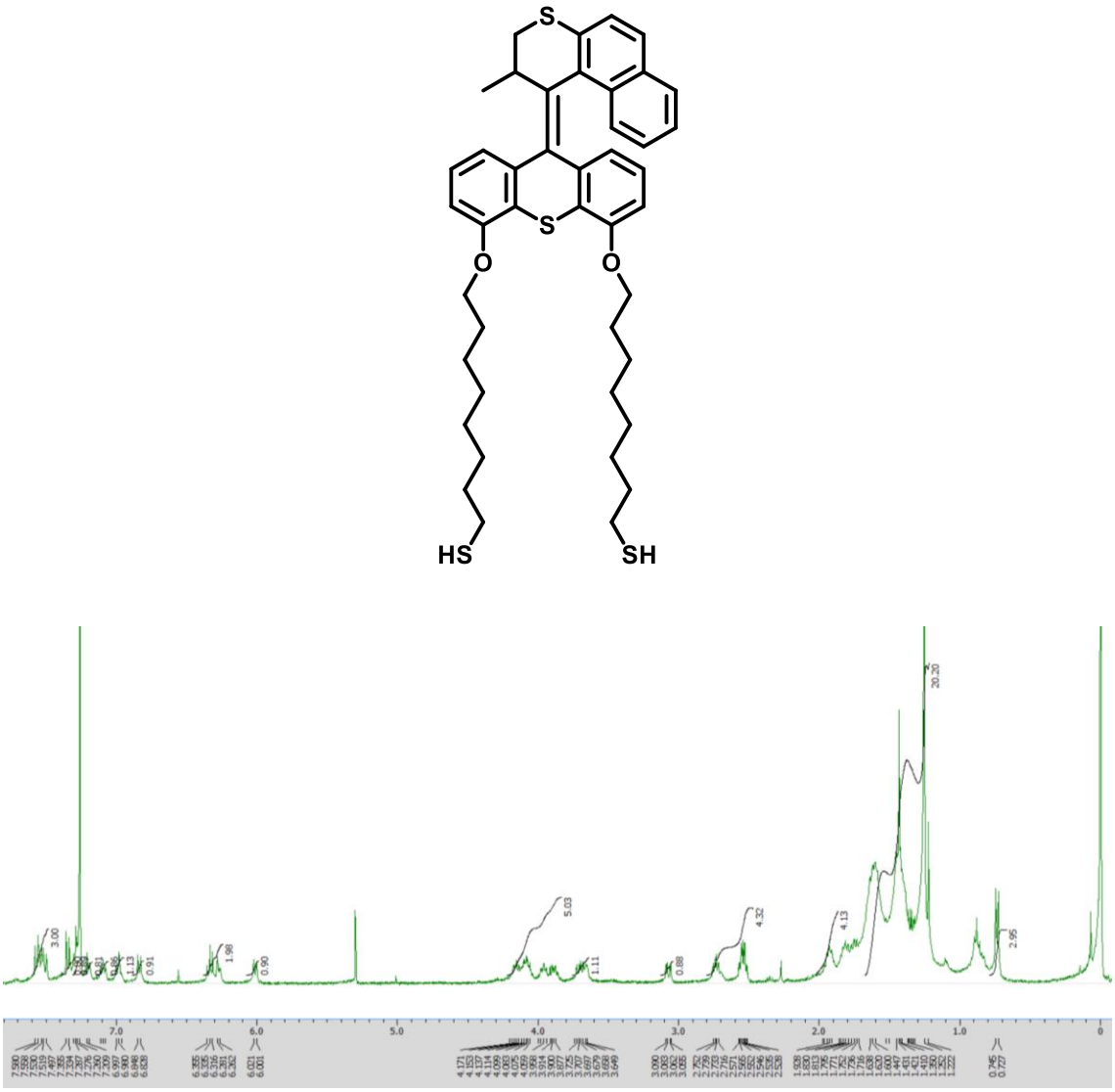

Fig. 3.7 ^{1}H NMR spectrum (400 MHz, $CDCl_3$) of the thiol-functionalized OCA.

The list of the chemical shifts in the unit of ppm is as follows; δ=0.74 (d, *J* = 7.0 Hz, 3H), 1.20-1.65 (m, 20H), 1.87-2.00 (m, 4H), 2.50-2.58 (m, 4H), 3.08 (dd, *J* = 11.4, 2.6 Hz, 1H), 3.72 (dd, *J* = 11.4, 7.3 Hz, 1H), 3.88-4.20 (m, 5H), 6.02 (dd, *J* = 8.0, 1.1 Hz, 1H), 6.26-6.36 (m, 2H), 6.84 (d, *J* = 8.0 Hz, 1H), 6.96-7.01 (m, 1H), 7.07-7.13 (m, 1H), 7.20 (d, *J* = 7.6 Hz, 1H), 7.26-7.32 (m, 1H), 7.35 (d, *J* = 8.1 Hz, 1H), 7.49-7.58 (m, 3H), the absorptions from the two SH protons were not observed.

Besides, I tested a 4-step chirality rotation of the target OCA in ethanol solution by circular dichroism (CD) measurements. Alternating light irradiation (λ = 465 nm) and heat application (80 ºC) would induce sequential unidirectional rotary processes accompanied by chiral switching between (*2'R*)-(*M*)-OCA and (*2'R*)-(*P*)-OCA. Here, I selected (*2'R*)-(*M*)-OCA as an initial compound. Thus, 180°-rotated structure is also expected to be (*2'R*)-(*M*)-OCA, and, in contrast, 90°- and 270°-rotated ones are (*2'R*)-(*P*)-OCA. I found that the CD spectrum of the initial, 180°- and 360°-rotated structures had similar structures, and also showed excellent mirror shapes against those of 90°- and 270°-rotated ones, clearly confirming a full chiral rotation of OCAs, which was totally consistent with the previous reports[73,77] (Fig. 3.3b) .

I next constructed an ordered monolayer of the OCAs through self-assembled scheme of the thiol-functionalized OCAs on gold surface, as schematically illustrated in Fig. 3.3c. Briefly, cleaned Si substrates covered by thick Ni and thin Au, whose thickness were 50 nm and 10 nm, respectively, were placed into an ethanolic solution consisting of 1 mM OCAs and left for a few days. After the incubation process, they were swiftly washed by ethanol to remove the unbound molecular residue (See Experimental section for more detailed information). Our atomic force microscopy (AFM) confirmed a highly homogeneous topography of self-assembled OCA monolayer on the substrate (Fig. 3.3d), in sharp contrast to the case of the film prepared by OCA-spin-coating methods in our previous study[73]. As displayed in the next section, the prepared SAM stably exhibits clear nonlinear current-voltage (*I-V*) profiles at all locations I measured, which can be considered as a hallmark of the successful formation of uniform SAM on the substrate (Fig. 3.8), in which raw dataset of nonlinear *I-V* curves of the SAM substrate and the linear *I-V* curve for a pristine substrate are presented.

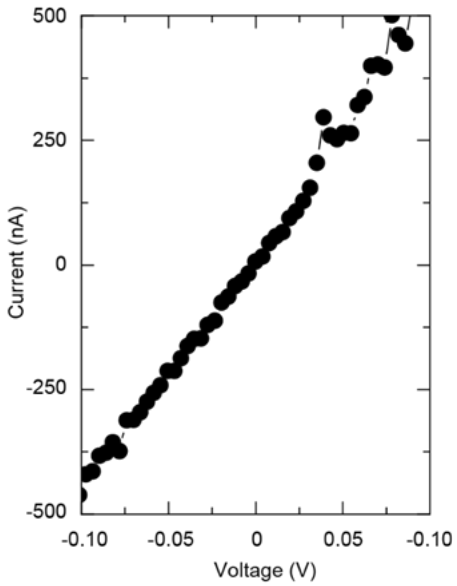

Fig. 3.8. Raw data of *I-V* curve for the pristine substrate without SAM. Observed current value reaches almost 500 nA with only applying 0.1 V.

3.4.2 Demonstration of the switchable spin filter with high stability.

Having established the high-quality SAM of chiral OCAs, I now return my attention to CISS-driven spin polarized current of the OCA-integrated magnetic substrate. To this end, I employ magneto-conductive atomic force microscopy (mC-AFM) that has been extensively used to get insight into spin-polarized current originating from CISS effect.[72,78–80] The schematic design of the experiments is shown in Fig. 3.9a. The ferromagnetic Ni layer works as a source of spin-polarized current whose spin direction is controlled by the orientation of magnetized spin in Ni. A top electrode of conductive diamond-coated Si tip scanned *I-V* profile of the prepared SAM of OCAs. Note that in my setup, a permanent magnet placed underneath the substrate can *in-situ* control the direction of Ni magnetization, enabling us to measure *I-V* profiles without moving the tip *x-y* location between up- and down-magnetized conditions (see Experimental method section).

Giving that the current path in AFM measurements is so sensitive to environments surrounding molecules (which actually manifests itself in large error bars observed in *I*-*V* curves), the comparison of the *I*-*V* profiles between opposite magnetized conditions free from tip-positional ambiguity is a significant advantage, which was indeed not achieved in our previous study.[73] In general, owing to the CISS effect, the transmission probability of electrons through chiral molecules depends on the orientation of polarized electron spin. I can thus evaluate a spin-polarization efficiency (or spin-filtering ability) of the chiral OCAs through a discrepancy in the measured current at a particular bias voltage between the situations where the Ni spins are aligned either parallel or antiparallel to the direction of the current. Furthermore, a sign of the difference in the current between the two magnetized directions also gives insight into whether the measured OCAs are up- or down-spin selective.

I selected (*2'R*)-(*M*)-OCA as a starting compound. The two-fold rotational symmetry along the central alkene is lost by anchoring the molecule, so full 360º rotation can be tested. The observed current in the initial (*2'R*)-(*M*)-OCA is measurably larger with Ni spin pointing up (*S*-pole) compared with that with spin pointing down (*N*-pole), confirming its up-spin-selective nature (Fig. 3.9b). I then switched its chirality in sequence between (*2'R*)-(*P*)-OCA and (*2'R*)-(*M*)-OCA) by photoirradiation or heat application and measured *I*-*V* profiles in each step (Fig. 3.9a). The results are summarized in Fig. 3.9c-3.9f. At first glance, the relationship between the current with Ni spin up (*S*-pole) and spin down (*N*-pole) inverts with each chiral-switching step, unambiguously substantiating the multiple inverting of down- or up-spin selective ability, which is in line with the expected behaviors of the molecular-motor (Fig. 3.1). What should be emphasized here is that even after full 360º rotation of the chirality, a marked difference can be still resolved in *I*-*V* curves

between the conditions with up- and down-magnetized spins (Fig. 3.9f), which is qualitatively indicative of the high stability of the SAM.

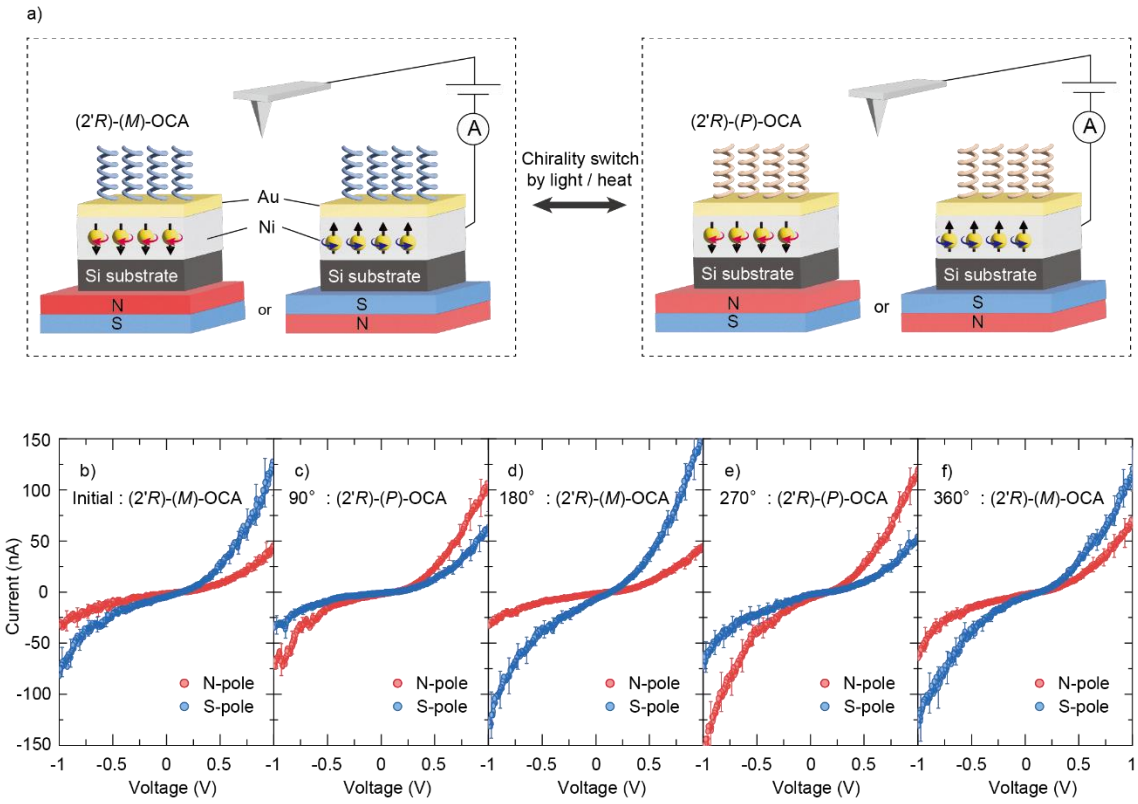

Fig. 3.9 a) Schematic illustration of mC-AFM measurements of the SAM of OCAs with using a ferromagnetic substrate. b-f) The observed *I*–*V* profiles under the condition of *N*-pole up or *S*-pole up for each-chirality step. At least 50 *I*–*V* curves were recorded and averaged for each handedness and magnetic field orientation. Error bars in these plots represent standard error. The raw data before averaging is displayed in Fig. 3.10.

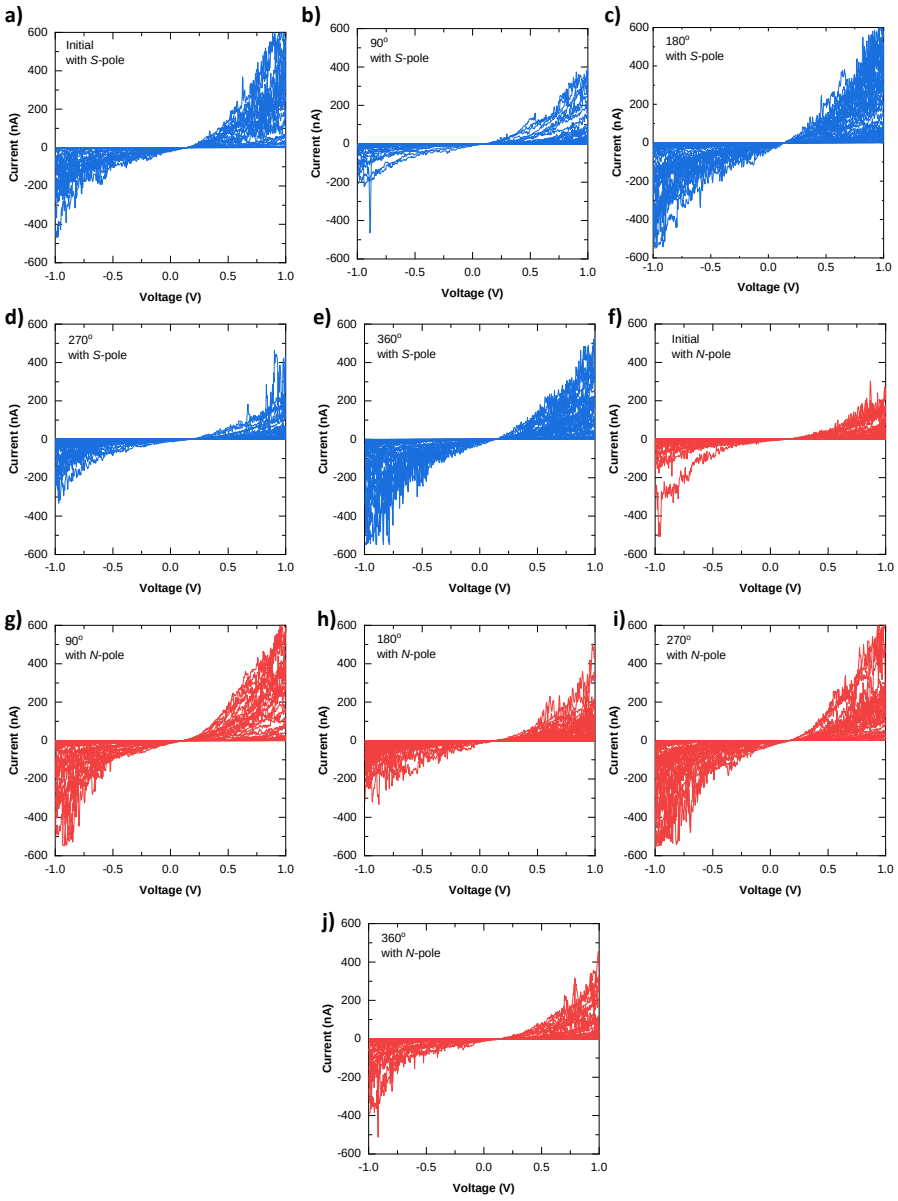

Fig. 3.10 Raw data of *I*-*V* curves for mC-AFM measurements with a condition of *S*-pole up (a-e, blue) and *N*-pole down (f-j, red). *I*-*V* curves for a) initial (*2'R*)-(*M*)-OCA, and those after b) 90°, c) 180°, d) 270°, and e) 360°-rotated step are displayed, respectively.

To further quantify the detected spin-polarization efficiency, it is convenient to consider a spin polarization (SP) rate by introducing a quantity of

$$\mathrm{SP}\ (\%) = \frac{I_{\mathrm{down}} - I_{\mathrm{up}}}{I_{\mathrm{down}} + I_{\mathrm{up}}} \times 100, \qquad (3.\ 1)$$

where I_{down} and I_{up} represent the currents measured for the magnetic field pointing down or up, respectively. The estimated SP rates for all rotation steps as a function of biased voltage are plotted in Fig. 3.11a, and exhibit two noteworthy features. First, the observed SP values in each chirality are approximately 25-60 % which are comparable or even larger to the previous study, reflecting its highly efficient SP ability inherent to the chiral OCAs.[73] Second, more importantly, the absolute values of SP estimated at each rotation step remain almost unchanged from the initial value even after multiple chiral rotations, quantitatively demonstrating its extremely durable functionality as spin-filter (Fig. 3.11b). As I have mentioned already, the stability against the chiral switching by external stimuli is ascribed to the covalent bond chemically fixing the OCAs to the Au layer. All of the above observations point to highly controllability and stability of the present CISS-based spin-switchable system.

Nevertheless, I note that intrinsic spin-filtering ability arising from chiral molecules is not a definitive assignment of the observed spin dependent phenomena. The role of several interfaces composed of Ni/Au/chiral molecules/AFM tip, that are inevitably involved in mC-AFM measurements, cannot be ruled out completely, which should be carefully clarified in future works.

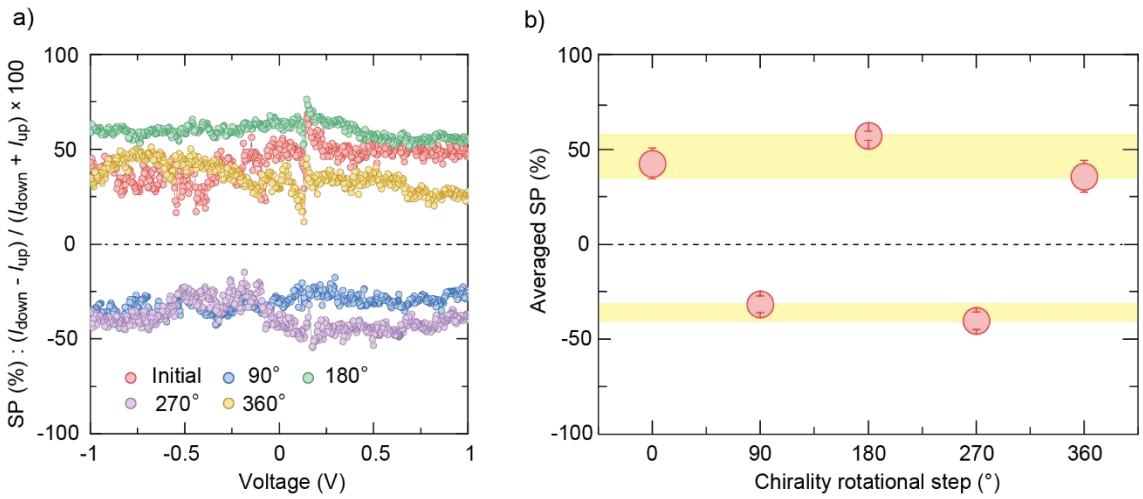

Fig. 3.11 a) Biased voltage dependence of the SP value evaluated from the dataset in Fig. 3.9b-3.9f. b) The averaged SP values are plotted as a function of chirality-rotational step. The statistical average is calculated by using the SP values in the range of +0.5 to +1 V and -0.5 to -1 V. The error bars show the standard deviations of the fitting.

3.4.3 Enhanced SP efficiency of OCA molecules by mixing with C_8 alkanethiol.

In general, van der Waals interaction between molecules plays a vital role in forming densely packed SAM with a highly ordered structure.[81] Indeed, molecules with longer alkyl chain in which the interaction is more relevant than in shorter molecules are revealed to be more easily self-assembled into an ordered structure.[81] However, this basic strategy for SAM deposition is seemingly incompatible with my OCA molecules; their relatively bulky head groups prevent the underneath C_8 alkyl chains from approaching together, possibly resulting in a disordered structure (Fig. 3.12a). A possible approach to avoid this problem is to accommodate a medium through which van der Waals force effectively interacts between neighboring OCAs, for instance, by introducing additional simple C_8 alkanethiols (1-Octanethiol) as a spacer[82] (Fig. 3.12b). If this method works, one expects that the stereo architecture of OCA layer can be more ordered, then

enhancing the SP efficiency per single OCA (Fig. 3.12b). With this working hypothesis, I prepared a mixed SAM of OCA and C_8 alkanethiol with varying the mixing ratio to examine its impact on resultant SP rates.

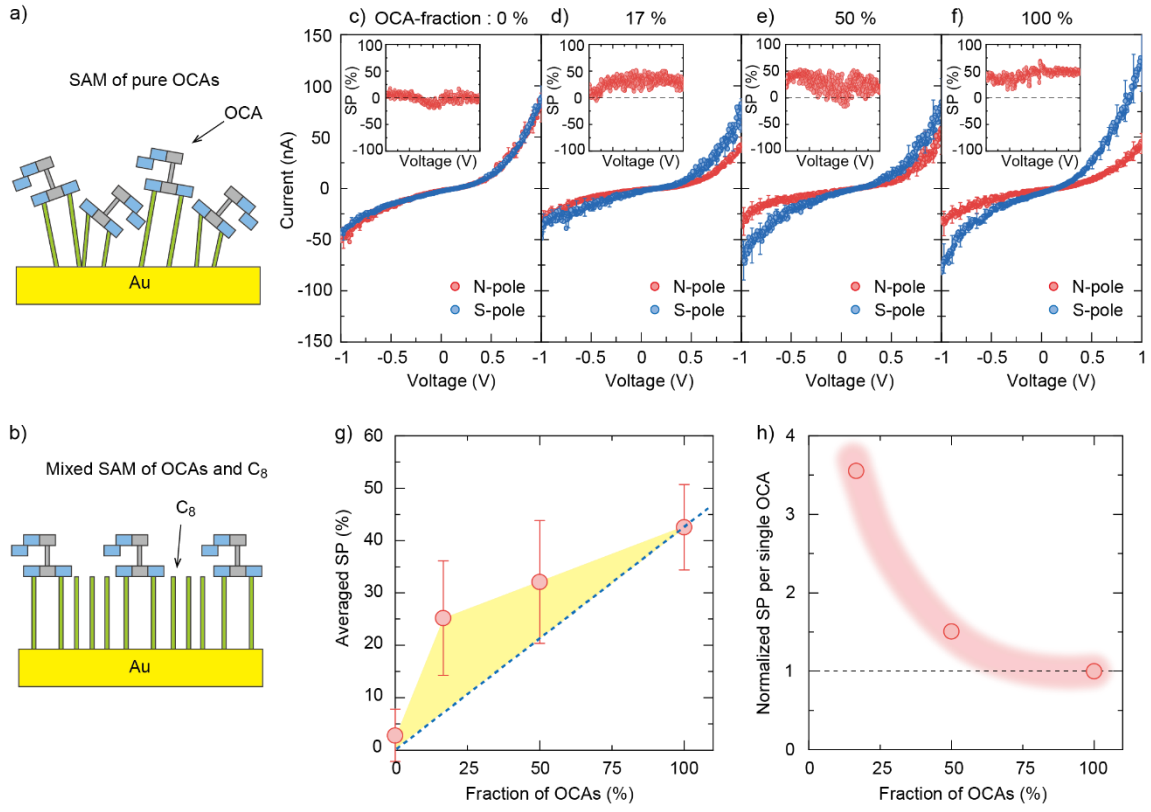

Fig. 3.12 a, b) Schematic representations of disordered SAM of pure OCAs and ordered SAM of mixed OCA and C_8 alkanethiol, respectively. C, d, e, f) *I-V* profiles of the mixed SAMs; the fractions of OCAs are 0 % (namely, pure C_8), 17%, 50 %, and 100 % (pure OCAs), respectively. Inset represents the evaluated SP value as a function of voltage for each mixture ratio. The raw data before averaging is displayed in Fig. 3.14 g) Deduced averaged SP rates against the fraction of OCAs. Blue dashed line corresponds to a linear extrapolation to zero SP value. Error bars are standard deviations. h) Normalized effective SP per a single OCA as a function of the fraction of OCAs, with an assumption that the current passes through all the molecules in equal probability. Note that the effective SP for pure C_8 system cannot be defined.

I here investigated four SAMs with a different mixture ratio of (*2'R*)-(*M*)-OCAs and C_8-alkanethiol: the fraction of OCAs of these systems are 0 % (pure C_8-alkanethiol), 17 %, 50 %, and 100 % (pure (*2'R*)-(*M*)-OCA), respectively. I used the original ratio of the two molecules in the bulk solution as the resultant ratio of the mixed SAM on the surface. Note that since the nominal mixture ratio of OCA against C8 is largely varied from 100 % to 0 %, a possible uncertainty about the actual mixture ratio of the SAM, at most a few percents, if any, does not influence the overall trends described below. Figs. 3.12c-3.2f display the obtained *I*-*V* curves for the four SAMs. I note that the observed current values tend to slightly decrease with lowering the concentration of OCAs (Figs. 3.12d-3.12f), which is explainable by taking the charge injection barrier to OCA from the electrode into account.

To clearly explain the charge injection barrier to OCA from the electrode into account, the fraction of OCA molecules dependence of the electric current will be carefully discussed. A diameter of the AFM tip (100-200 nm) is much larger than the width of the molecule (the order of 0.1 nm), forcing us to consider that the observed current reflects not a single molecule but a considerable number of molecules. With this condition, the following two factors can affect the charge transport through the OCA and C_8 alkanethiol; (i) tunneling rate and (ii) charge injection barriers. As for the first factor, the OCA is longer than C_8, thus indicating that the electron tunneling rate through OCA is lowered compared with the case for C_8. If this factor is dominant, observed current value would *increase* with decreasing the fraction of OCA in my mixed SAM.

In contrast, the second factor leads to the opposite tendency. Whereas HOMO/LUMO of simple alkanethiol is in general located far from Fermi level of conventional metal [83], HOMO or LUMO of the family of OCA is expected to be closer to the Fermi level (For example, see Ref.

[84]). It means that the charge injection barrier between OCA and electrode is more suppressed compared with that between C_8 and electrode. Thus, I can expect that observed current value would *decrease* with decreasing the fraction of OCA. As a consequence, resultant current can either increase or decrease as the fraction of OCA gets smaller, depending on which factor is more dominant.

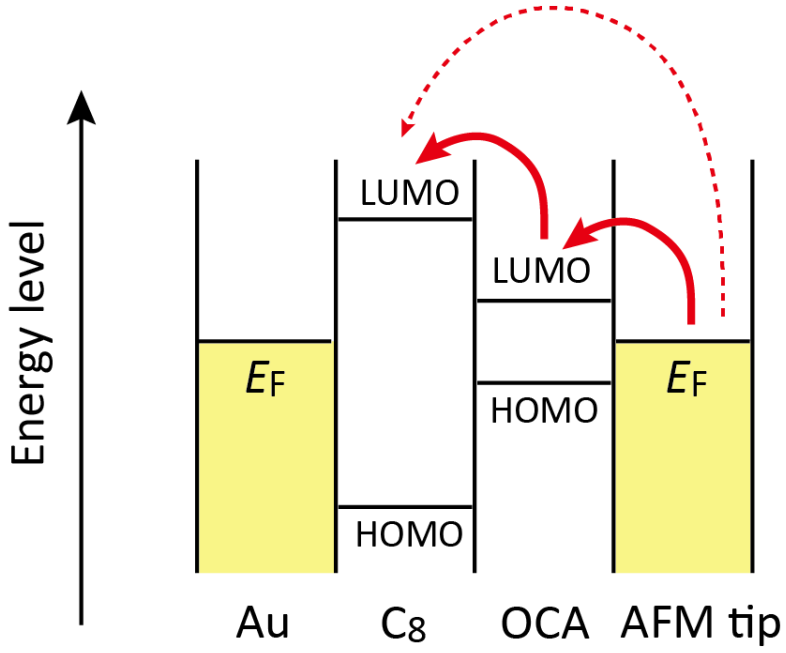

Fig. 3.13 Schematics of possible tunneling processes through both C_8 and OCA. Sequential hopping mediated by OCA is more likely than a direct hopping from tip to C_8, considering their energy levels.

With this point in mind, let me revisit the experimentally observed tendency in Figs. 3.12(c-f), that is, current is slightly reduced with decreasing the fraction of OCA. It implies that the second factor, charge injection barrier, is more relevant in my measurements than the first one is. Within this picture, I assume that the electrical current passes through both OCA and C_8 alkanethiol. To

clearly explain, there is a large difference in energy between HOMO or LUMO of alkane and Fermi level of the electrode. Therefore, when OCA is placed near the alkane, the charge tends to pass through the OCA that gives an intermediate HOMO or LUMO level closer to the Fermi level, instead of directly transforming into the alkane (Fig. 3.13). In other words, the spin filtering capability of chiral OCA may influence the alkanes closely located to the OCA, possibly resulting in an enhanced spin polarization. With this assumption, one can calculate the spin polarization per OCA molecule in the (OCA+C_8) film by introducing the detected spin polarization divided by the OCA fraction, as a phenomenological parameter that can be helpful in practical applications. The evaluated spin polarization per OCA molecule increases with dilution, as I previously discussed in Fig. 3.12.

The corresponding SP values based on Eq. (3.1) are shown in the insets of Figs. 3.12c-3.12f, and then the averaged SP are plotted against the fraction of OCAs (Fig. 3.12g). If my hypothesis is not valid, that is, SP rate is determined not by the stereo architecture of OCAs but simply by the number of OCA molecules, the OCA-fraction dependence of the SP rates would follow a linear relationship to zero SP value (a blue-dashed line in Fig. 3.12g). Remarkably, however, the observed SP rates clearly deviate from the linear relationship (highlighted by yellow-shaded region in Fig. 3.12g), and the SP of the 17 % fraction of OCAs is still comparable with that of pure OCAs. This notable signature strongly suggests that each OCA molecule more efficiently generates spin-polarized current in the form of mixed SAM. The claim becomes more stringent in the plot of the SP value divided by the fraction of OCAs that is a good measure for the SP efficiency per single OCA molecule, namely effective SP rate (Fig. 3.12h). Especially the case of 17 % fraction of OCA is revealed to show more than three times larger value than that of pure OCAs (Fig. 3.12h). These results lead us to conclude that the stereo architecture of OCA layer is

dramatically improved by the introduction of a spacer of C_8 alkanethiol, more efficiently contributing to spin-filtering effect, well in line with my hypothesis. I also note that the pure C_8 system exhibits no SP, assuring that the evaluation of SP value in my measurements is highly accurate and that the systematic variation in SP for different mixture ratios is intrinsic. The enhanced effective SP by the mixed SAM can offer an additional advantage for future practical application of OCA; even the SAM of diluted OCAs potentially exhibits a considerable spin filtering functionality, and thus is very likely to be compatible with the cost-reduction of the device.

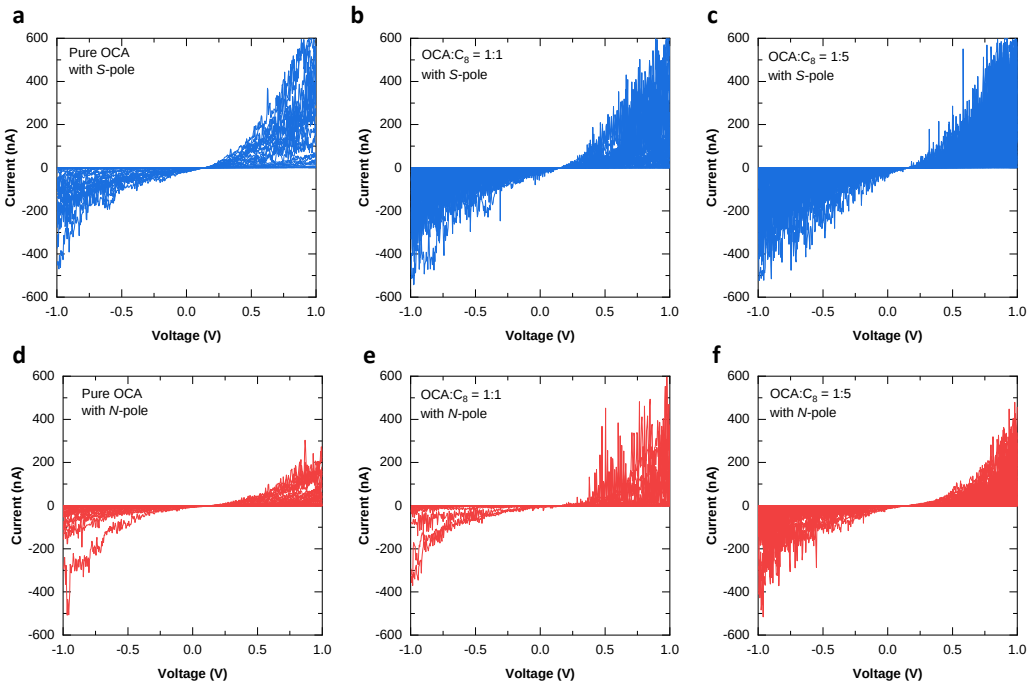

Fig. 3.14 Raw data of *I-V* curves for the substrates of mixed SAM of OCA and C_8 alkanethiol. a) and d) A pure OCA (the fraction of OCA is 100 %) with *S*- and *N*-pole up, respectively. b) and e) Mixed SAM with a ratio of OCA:C_8 = 1:1 (the fraction of OCA is 50 %) with *S*- and *N*-pole up, respectively. c) and f) Mixed SAM with a ratio of OCA:C_8 = 1:5 (the fraction of OCA is 17 %) with *S*- and *N*-pole up, respectively.

3.5 Conclusions

I have successfully developed SAM of thiol-functionalized chiral molecular motor OCAs, whose chirality can be externally switched upon photoirradiation and heat application, for the first time. I demonstrated that the CISS-induced spin polarization in the system inverts its direction by rotating the molecular chirality in repeatable and highly stable manners. Remarkably, even after multiple switching of the chirality, the amplitude of the spin polarization persists in a quantitative level. This critical feature is brought about by the formation of covalent bonds robustly connecting SAM to the substrate, and should be distinguished from that of our previous OCA device without covalent bonds in which the amplitude of spin polarization gradually deteriorates after a single chiral switching[73] (The situation seems similar with the first-generation OCA systems although the details are not described in ref.[85]). Furthermore, I tailored a stereo architecture of the OCAs layer by mixing C_8 alkanethiol, giving a new route to enhance the efficiency of spin polarization per single OCA; only 17% fraction of OCA can exhibit an appreciable spin polarization comparable with that of 100% fraction of OCA. The present experimental investigations report the creditable feasibility study towards the versatile CISS-based spintronic molecular devices with controllability, durability, and high efficiency.

Finally, promising future research direction based on the present study would be a realization of two-terminal device with SAM of chiral OCAs and its integration into Magnetoresistive Random Access Memory (MRAM) as a possible practical form of CISS-based device. Tip-enhanced plasmon and local Joule heating are potentially available to locally and sequentially rotate the molecular chirality of OCAs in the CISS-based MRAM devices.[86–88]

Chapter 4

Engineering Surface Spin Based on Chiral Dielectric Material

Authors contributing to this study: Ruttapol Malatong, Takuro Sato, Hiroshi M. Yamamoto

4.1 Abstract

Triglycine sulfate (TGS), one of the most known ferroelectric materials, has been intensively researched, presenting the ferroelectric phase below the transition temperature. Particularly, TGS as ferroelectric chiral material would raise questions for chiral-induce spin selectivity (CISS) effect, in which charge transport in macroscopic ferroelectric material is generated by displacement current. If CISS in ferroelectric chiral material could be observed, CISS mechanism, which is now still controversial, would be able to verify with more unambiguous answers. Through this topic, TGS-based devices, which can externally be switched on its chirality by poling process, were studied in the quest for alternating current-induced CISS effect to detect spin accumulation on the surface. This study would open a new playground in understanding CISS effect and in the characterization of ferroelectric chiral material.

4.2 Introduction

Chirality characterizes right and left two enantiomers that its mirror image does not overlap. It is a crucial and fundamental notion in numerous areas such as biology, chemistry, and physics.[89] In terms of symmetry language, chirality, lacking both inversion and mirror symmetry,

has recently remarkably attracted attention due to its unique ability to tie the electron motion to its spin angular momentum. Particularly, spin transport through chiral organic materials has recently received considerable interest as the new generation electronic devices. Although organic molecules exhibit negligible spin-orbit interaction (SOI) because of the constituent light elements, the recent finding of unexpectedly large spin-polarized electron transport through chiral molecules, which referred to as chiral-induced spin selectivity (CISS) effect, suggests a novel platform of using organic materials for spintronic applications.[8–13]

Thus far, most CISS studies have focused on chiral metals or insulating organic monomolecular layers to experimentally discuss spin-polarized current. [27–32] Then a fundamental question arises on CISS effect in chiral ferroelectric materials because charge transport in macroscopic ferroelectric materials is only possible with displacement current. Therefore, an emergent spin-polarized current, if any, is likely due to the displacement current. Based on chirality and magnetism, chiral ferroelectrics have first represented by triglycine sulfate (TGS) which has been obtained in magnetochiral anisotropy (MChA).[64] TGS have opened a whole new window on ferroelectric material since then. TGS based on ferroelectric chiral material that is able to observe MChA, it is also possibly reasonable to hypothesize CISS associated to chirality and magnetism by detecting spin accumulation on the surface.

Triglycine sulfate (TGS) crystal consists of achiral phase above transition temperature, and it will be chiral phase below transition temperature. A unique handedness can be characterized throughout the entire crystal by poling process (decreasing temperature from the achiral high-temperature phase) with electric field parallel to the (polar) y-axis.[65,90,91] In this work, I study the alternating current (AC)-induced CISS effect in TGS under AC current excitation by detecting the spin accumulation with direct current (DC) voltage at the interface. The results demonstrate the

antisymmetric signal profiles as the function of the magnetic field. Unfortunately, The TGS-based devices with different handedness, switched by poling process exhibit similar behavior. I initially conclude that this phenomenon is not probably due to CISS, in which spin accumulation could not be detected, even the chirality is switched. However, the possible antisymmetric curves and why CISS undetected will be discussed in detail. Through this work, if the ferroelectric materials are brought to utilize for CISS effect, it would establish the novel concept for spintronic devices.

4.3 Experimental section

4.3.1 Synthesis of triglycine sulfate (TGS) crystal

TGS crystals were synthesized in aqueous solution following a literature procedure.[65] First, 130 g of glycine and 30 mL of sulfuric acid with molar concentration ratio 3:1 were dissolved and stirred in 500 mL of distilled water. The reaction mixture was subsequently heated at 50 ^{o}C to avoid decomposition of the salt for 30 min. Finally, TGS solution was safely kept and grown by slowly evaporating the solvent at room temperature.

4.3.2 Preparing TGS-based device covered by Au/TGS/Ni and Au/TGS/Au

TGS crystals were cut into cross-section perpendicular to the *b*-axis with thickness of ~500 μm and then washed in hexane and dried. The TGS crystals were then swiftly transferred to an electron-beam evaporation system. Electrodes as Ni and Au layers, whose thickness are both 50 nm were evaporated at rate of ~0.2 Å s^{-1} with a base pressure of approximately 10^{-5} Pa (the device structure is depicted in Fig. 4.1).

4.3.3 Poling process

After the deposition of electrodes on TGS, the poling process was performed in a He atmosphere by using a physical property measurement system (PPMS) (Quantum Design). Under sweeping temperature from 340 K to 300 K, voltages of +150 V or −150 V were applied between the electrodes to change the chirality using the source meter (Keithley 2636A), after which monodomain chiral ferroelectric phase is expected to appear. The chiral switching was obtained by measuring pyroelectric coefficient with increasing temperature from 300 K to 340 K.

4.3.4 Detection of the accumulated spin on the surface

In order to detect the accumulated spin on the surface, an alternating voltage of 7 V with frequency of 100 kHz was applied by using a function generator (NF Corporation, WF1947). A direct current (DC) voltage nanovoltmeter (Keithley 2182A) was connected, and devices were tested. The measurements were performed in a He atmosphere by using a physical property measurement system (PPMS) (Quantum Design).

4.4 Results and Discussion

4.4.1 Pyroelectric measurements of TGS

To study CISS effect, a polling process to switch chirality was first studied by pyroelectric measurements. The relationship between pyroelectric current (i_P) and polarization (P_S) is demonstrated in the equation below.

$$i_P = \frac{\mathrm{d}Q}{\mathrm{d}t} = A\frac{\mathrm{d}P_S}{\mathrm{d}t} = A\frac{dP_S}{dt}\frac{\mathrm{d}T}{\mathrm{d}t} \qquad \textbf{Equation 4.1}$$

$$P_S = \frac{1}{\mathrm{A}}\frac{1}{\frac{\mathrm{d}T}{\mathrm{d}t}}\int i_P \mathrm{d}T \qquad \textbf{Equation 4.2}$$

where A is the crystal area and (1/(d*T*/d*t*)) is the heating rate of 0.3 K s^{-1}

Based on equation 4.1, polarization of TGS could not be experimentally measured, I rather measured pyroelectric current and subsequently measured polarization from the equation 4.2 by integrating equation 4.1. The origin of pyroelectric current is temperature dependence of the polarization. Meaningly, with increasing temperature, polarization decreases, which influences current releasing from TGS and subsequently pyroelectric current is measured.

The TGS sample was slowly cooled from 340 K to 300 K under electric field, and subsequently measured pyroelectric current by increasing temperature from 300 K to 340 K. As can be seen from Fig. 4.1a, under cooling with positive polarity, there was no signal appearing at 300 K. Then increasing temperature until 323.29 K made the signal profile curve suddenly enhanced as the sharp peak structure which could be referred to as a transition temperature or curie temperature (T_c). After increasing temperature to 340 K, the signal became zero. Notably, the sharp characteristic peak implies that the microscopic phase suddenly changes to form the homogenous domains which is consistent with the previous work.[65,67,90] Besides, the polarization was also calculated based on pyroelectric current curves by integrating the pyroelectric current equation. As expected, no polarization appears above T_c confirming paraelectric nature (see in Fig. 4.1c). On the other hand, polarization became finite below T_c corresponding to ferroelectric phase. In case of changing polarity to negative, the signal profile curves in both pyroelectric current and polarization were opposite to the positive polarity (see in Fig. 4.1d). As a result, two TGS-based devices with opposite poling processes were observed which correspondingly determined the

opposite handedness of chirality. Also, I found that at 323.29 K shows the peaks of the transition temperature or curie temperature (T_c), revealing that at temperature higher than T_c, the TGS is achiral with space group $P2/m$, whereas at temperature lower than T_c the mirror symmetry is broken and the TGS became chiral with space group $P2_1$.[61,62] Therefore, this measurement confirmed that the chirality of TGS was switched by poling process, being observed from pyroelectric measurements.

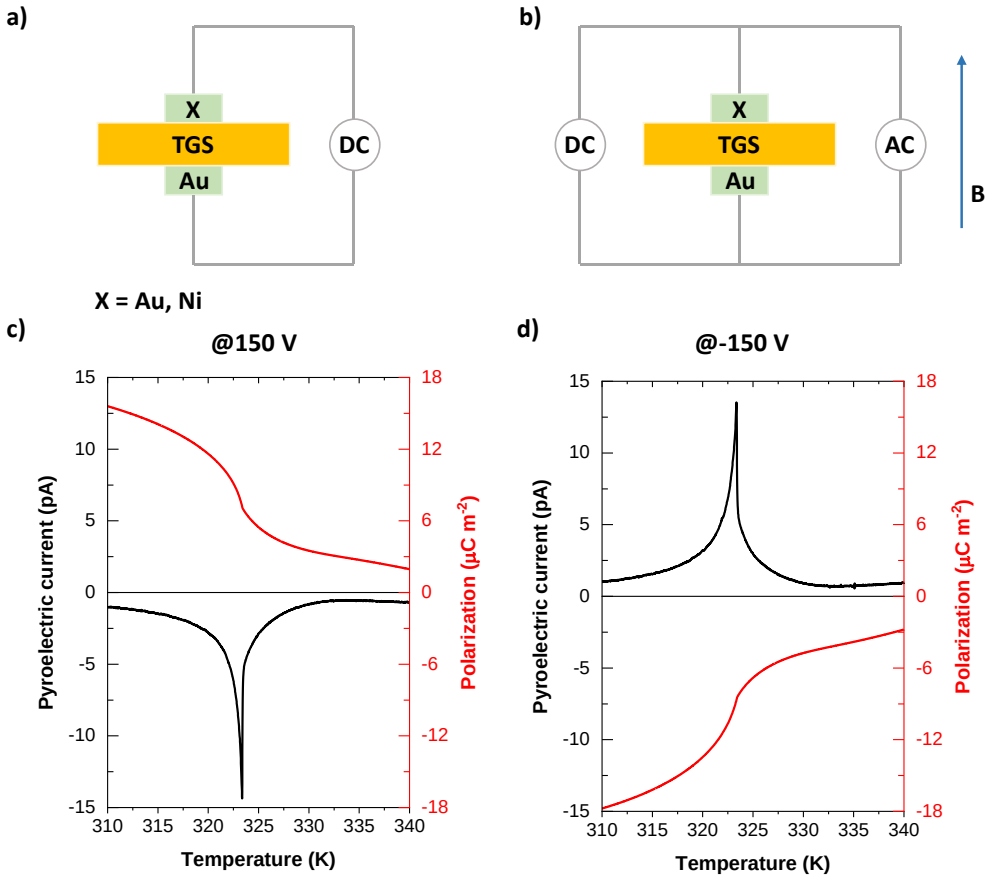

Fig. 4.1 a) device structure for poling process, b) device structure for CISS detection, c) and d) pyroelectric current and polarization curves by positive (+150 V) and negative (-150 V) excitation for poling process, respectively

4.4.2 CISS verification from detection of the accumulated spin on the surface

Having switched chirality by poling process, next I studied alternating current (AC)-induced CISS effect in TGS under AC excitation by detecting the spin accumulation with direct current (DC) voltage at the interface. First, I established the device configuration as shown in Fig. 4.1b. I prepared different device structures as follows: Au (50 nm)/TGS (0.5 mm)/Au (50 nm), and Ni (50 nm)/TGS (0.5 mm)/Au (50 nm), respectively. The first device without ferromagnetic layer (Ni) was measured with DC voltage at the interface as the function of magnetic field by applying AC with V_{rms} of 7 V, 100 kHz with temperature dependence.

As can be seen from Fig. 4.2a and 4.2b, symmetric curves typically showed up in the magnetic field dependence, in which magnetoresistance has a symmetric part (even component against magnetic field). In CISS detection, I therefore focus on asymmetric part (odd component) by decomposing the even component with antisymmetrized data (see in Fig. 4.2c and 4.3d). From my hypothesis, if no CISS effect exists in the system, asymmetric curve would be unable to appear. These devices, however, demonstrate the antisymmetric signal profiles with temperature dependence close to transition temperature (323.29 K) as the function of the magnetic field. Thus far, I have no idea why antisymmetric behaviors which are the same in both handedness appears to these devices. Nevertheless, I have additional setup by adding Ni as the electrode to detect spin accumulation to verify CISS with opposite antisymmetric curve anticipated to be observed depending on chirality.

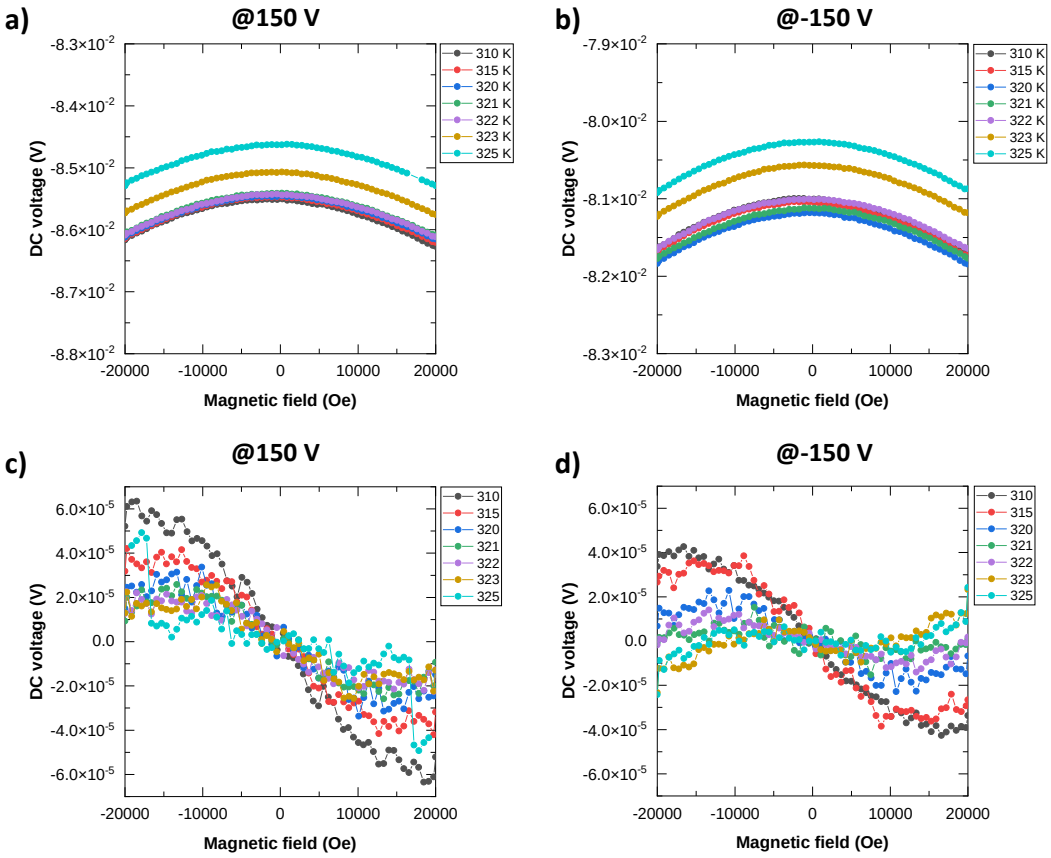

Fig. 4.2 a) and b) Symmetric curves of DC voltage as the function of magnetic field by poling process at +150 V and -150 V, respectively, c) and d) Asymmetric curves of DC voltage as the function of magnetic field by poling process at +150 V and -150 V, respectively [Device structure: Au (50 nm)/ TGS (0.5 mm)/ Au (50 nm)].

I used the ferromagnetic layer (Ni) as spin detector (see in Fig. 4.1b) to verify CISS effect. The measurement was the same as the previous device. After antisymmetrized data from Fig. 4.3a and 4.3b, I found that opposite handedness still exhibited the antisymmetric curves with the same slope-sign curves (see in Fig. 4.3c and 4.3d). This phenomenon is not likely due to CISS, and I

came to conclude that spin accumulation could not be detected, even if the chirality is switched. With this system, TGS-based devices to detect spin accumulation would probably not be able to obtain CISS effect.

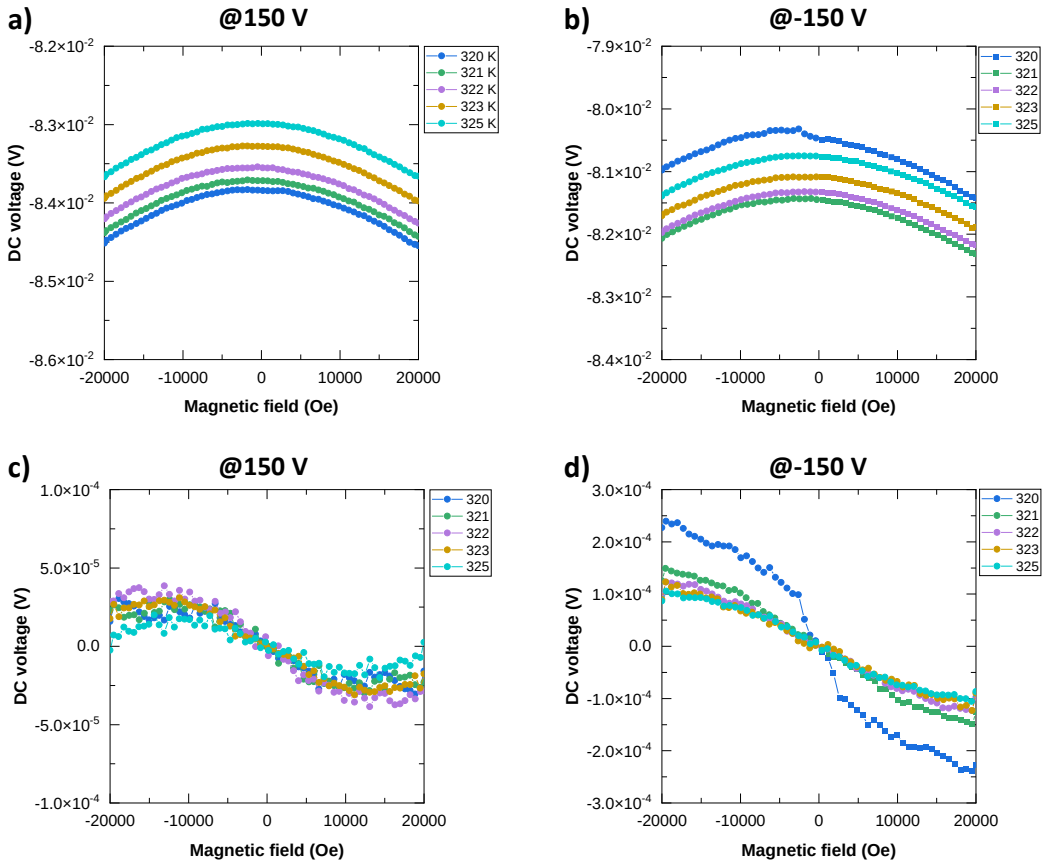

Fig. 4.3 a) and b) Symmetric curves of DC voltage as the function of magnetic field by poling process at +150 V and -150 V, respectively, c) and d) Asymmetric curves of DC voltage as the function of magnetic field by poling process at +150 V and -150 V, respectively [Device structure: Ni (50 nm)/ TGS (0.5 mm)/ Au (50 nm)].

Through these measurements, several possibilities why the signal cannot be obtained are hypothesized. Both electrodes covered onto the TGS have some different impurities which unexpectedly affect the interface. Another one is that CISS is probably a tiny intrinsic signal which is overwhelmed by the interfacial effect. To address these issues, cleaning homogeneous surface is desired which could increase the possibility to observe CISS effect from TGS-based devices.

4.5 Conclusions

Triglycine sulfate (TGS), a chiral ferroelectric material, was successfully synthesized and characterized to define handedness that can be switched by poling process under voltage excitation (+150 V and -150 V). With this system, the ferroelectric phase below transition temperature becomes chiral with space group $P2_1$. A signal peak of pyroelectric coefficient and polarization could be observed depending on the voltage excitation direction. TGS-based devices were subsequently measured to detect spin accumulation on surface. Unfortunately, the TGS-based devices with different handedness, switched by an opposite poling process, exhibited similar behavior to one another in the antisymmetric curve as the function of magnetic field. This phenomenon is not likely due to CISS, in which spin accumulation should be reversed if the chirality is switched. Because of the interfacial effect, CISS is probably screened and therefore, cleaning interface to create homogeneous structure is highly desired to observe CISS effect from TGS-based devices. If CISS in TGS as a chiral ferroelectric material could be verified, it would benefit and open a new window to obtain insight in understanding CISS as well as to develop spintronics devices in the future.

References

[1] S.-H. Yang, *Nat. Mater.* **2022**, *21*, 494.

[2] A. Manchon, H. C. Koo, J. Nitta, S. M. Frolov, R. A. Duine, *Nature Mater* **2015**, *14*, 871.

[3] J. Sinova, S. O. Valenzuela, J. Wunderlich, C. H. Back, T. Jungwirth, *Rev. Mod. Phys.* **2015**, *87*, 1213.

[4] K. Ishizaka, M. S. Bahramy, H. Murakawa, M. Sakano, T. Shimojima, T. Sonobe, K. Koizumi, S. Shin, H. Miyahara, A. Kimura, K. Miyamoto, T. Okuda, H. Namatame, M. Taniguchi, R. Arita, N. Nagaosa, K. Kobayashi, Y. Murakami, R. Kumai, Y. Kaneko, Y. Onose, Y. Tokura, *Nature Mater* **2011**, *10*, 521.

[5] J. C. R. Sánchez, L. Vila, G. Desfonds, S. Gambarelli, J. P. Attané, J. M. De Teresa, C. Magén, A. Fert, *Nat Commun* **2013**, *4*, 2944.

[6] V. M. Edelstein, *Solid State Communications* **1990**, *73*, 233.

[7] S.-H. Yang, *Nat. Mater.* **2022**, *21*, 494.

[8] R. Naaman, Y. Paltiel, D. H. Waldeck, *Acc. Chem. Res.* **2020**, *53*, 2659.

[9] B. Göhler, V. Hamelbeck, T. Z. Markus, M. Kettner, G. F. Hanne, Z. Vager, R. Naaman, H. Zacharias, *Science* **2011**, *331*, 894.

[10] R. Naaman, D. H. Waldeck, *Annual Review of Physical Chemistry* **2015**, *66*, 263.

[11] K. Michaeli, V. Varade, R. Naaman, D. H. Waldeck, *J. Phys.: Condens. Matter* **2017**, *29*, 103002.

[12] R. Naaman, D. H. Waldeck, *J. Phys. Chem. Lett.* **2012**, *3*, 2178.

[13] R. Naaman, Y. Paltiel, D. H. Waldeck, *J. Phys. Chem. Lett.* **2020**, *11*, 3660.

[14] S. Dalum, P. Hedegård, *Nano Lett.* **2019**, *19*, 5253.

[15] F. Evers, A. Aharony, N. Bar-Gill, O. Entin-Wohlman, P. Hedegård, O. Hod, P. Jelinek, G. Kamieniarz, M. Lemeshko, K. Michaeli, V. Mujica, R. Naaman, Y. Paltiel, S. Refaely-Abramson, O. Tal, J. Thijssen, M. Thoss, J. M. van Ruitenbeek, L. Venkataraman, D. H. Waldeck, B. Yan, L. Kronik, *Advanced Materials* **2022**, *34*, 2106629.

[16] D. H. Waldeck, R. Naaman, Y. Paltiel, *APL Materials* **2021**, *9*, 040902.

[17] M. Kettner, V. V. Maslyuk, D. Nürenberg, J. Seibel, R. Gutierrez, G. Cuniberti, K. H. Ernst, H. Zacharias, *Journal of Physical Chemistry Letters* **2018**, *9*, 2025.

[18] B. Göhler, V. Hamelbeck, T. Z. Markus, M. Kettner, G. F. Hanne, Z. Vager, R. Naaman, H. Zacharias, *Science* **2011**, *331*, 894.

[19] M. Suda, Y. Thathong, V. Promarak, H. Kojima, M. Nakamura, T. Shiraogawa, M. Ehara, H. M. Yamamoto, *Nature Communications* **2019**, *10*, 1.

[20] P. C. Mondal, N. Kantor-Uriel, S. P. Mathew, F. Tassinari, C. Fontanesi, R. Naaman, *Advanced Materials* **2015**, *27*, 1924.

[21] K. Senthil Kumar, N. Kantor-Uriel, S. P. Mathew, R. Guliamov, R. Naaman, *Physical Chemistry Chemical Physics* **2013**, *15*, 18357.

[22] S. Mishra, A. K. Mondal, E. Z. B. Smolinsky, R. Naaman, K. Maeda, T. Nishimura, T. Taniguchi, T. Yoshida, K. Takayama, E. Yashima, *Angewandte Chemie - International Edition* **2020**, *59*, 14671.

[23] F. Tassinari, D. R. Jayarathna, N. Kantor-Uriel, K. L. Davis, V. Varade, C. Achim, R. Naaman, *Advanced Materials* **2018**, *30*, 1.

[24] V. Kiran, S. P. Mathew, S. R. Cohen, I. Hernández Delgado, J. Lacour, R. Naaman, *Advanced Materials* **2016**, *28*, 1957.

[25] A. Inui, R. Aoki, Y. Nishiue, K. Shiota, Y. Kousaka, H. Shishido, D. Hirobe, M. Suda, J. I. Ohe, J. I. Kishine, H. M. Yamamoto, Y. Togawa, *Physical Review Letters* **2020**, *124*, 166602.

[26] A. Kumar, E. Capua, M. K. Kesharwani, J. M. L. Martin, E. Sitbon, D. H. Waldeck, R. Naaman, *Proceedings of the National Academy of Sciences of the United States of America* **2017**, *114*, 2474.

[27] R. A. Rosenberg, D. Mishra, R. Naaman, *Angewandte Chemie - International Edition* **2015**, *54*, 7295.

[28] T. J. Zwang, S. Hürlimann, M. G. Hill, J. K. Barton, *Journal of the American Chemical Society* **2016**, *138*, 15551.

[29] G. Koplovitz, D. Primc, O. Ben Dor, S. Yochelis, D. Rotem, D. Porath, Y. Paltiel, *Advanced Materials* **2017**, *29*, DOI 10.1002/adma.201606748.

[30] O. Ben Dor, S. Yochelis, S. P. Mathew, R. Naaman, Y. Paltiel, *Nature Communications* **2013**, *4*, 1.

[31] V. Kiran, S. R. Cohen, R. Naaman, *Journal of Chemical Physics* **2017**, *146*, DOI 10.1063/1.4966237.

[32] C. Kulkarni, A. K. Mondal, T. K. Das, G. Grinbom, F. Tassinari, M. F. J. Mabesoone, E. W. Meijer, R. Naaman, *Advanced Materials* **2020**, *32*, 1.

[33] J. Fransson, *J. Phys. Chem. Lett.* **2019**, *10*, 7126.

[34] T. P. Fay, D. T. Limmer, *Nano Lett.* **2021**, *21*, 6696.

[35] G.-F. Du, H.-H. Fu, R. Wu, *Phys. Rev. B* **2020**, *102*, 035431.

[36] A. G. Volosniev, H. Alpern, Y. Paltiel, O. Millo, M. Lemeshko, A. Ghazaryan, *Phys. Rev. B* **2021**, *104*, 024430.

[37] Y. Wu, J. E. Subotnik, *Nat Commun* **2021**, *12*, 700.

[38] K. Ray, S. P. Ananthavel, D. H. Waldeck, R. Naaman, *Science* **1999**, *283*, 814.

[39] I. Carmeli, V. Skakalova, R. Naaman, Z. Vager, *Angewandte Chemie* **2002**, *114*, 787.

[40] M. Kettner, V. V. Maslyuk, D. Nürenberg, J. Seibel, R. Gutierrez, G. Cuniberti, K.-H. Ernst, H. Zacharias, *J. Phys. Chem. Lett.* **2018**, *9*, 2025.

[41] Z. Xie, T. Z. Markus, S. R. Cohen, Z. Vager, R. Gutierrez, R. Naaman, *Nano Lett.* **2011**, *11*, 4652.

[42] O. Ben Dor, N. Morali, S. Yochelis, L. T. Baczewski, Y. Paltiel, *Nano Lett.* **2014**, *14*, 6042.

[43] S. Ravi, *Superlattices and Microstructures* **2020**, *147*, 106688.

[44] D. Mishra, T. Z. Markus, R. Naaman, M. Kettner, B. Göhler, H. Zacharias, N. Friedman, M. Sheves, C. Fontanesi, *Proceedings of the National Academy of Sciences* **2013**, *110*, 14872.

[45] S. P. Mathew, P. C. Mondal, H. Moshe, Y. Mastai, R. Naaman, *Appl. Phys. Lett.* **2014**, *105*, 242408.

[46] M. Suda, Y. Thathong, V. Promarak, H. Kojima, M. Nakamura, T. Shiraogawa, M. Ehara, H. M. Yamamoto, *Nat Commun* **2019**, *10*, 2455.

[47] B. L. Feringa, *Acc. Chem. Res.* **2001**, *34*, 504.

[48] N. Koumura, E. M. Geertsema, M. B. van Gelder, A. Meetsma, B. L. Feringa, *J. Am. Chem. Soc.* **2002**, *124*, 5037.

[49] R. Naaman, D. H. Waldeck, Y. Paltiel, *Appl. Phys. Lett.* **2019**, *115*, 133701.

[50] T. S. Metzger, S. Mishra, B. P. Bloom, N. Goren, A. Neubauer, G. Shmul, J. Wei, S. Yochelis, F. Tassinari, C. Fontanesi, D. H. Waldeck, Y. Paltiel, R. Naaman, *Angewandte Chemie International Edition* **2020**, *59*, 1653.

[51] R. A. Rosenberg, M. Abu Haija, P. J. Ryan, *Phys. Rev. Lett.* **2008**, *101*, 178301.

[52] K. Banerjee-Ghosh, O. Ben Dor, F. Tassinari, E. Capua, S. Yochelis, A. Capua, S.-H. Yang, S. S. P. Parkin, S. Sarkar, L. Kronik, L. T. Baczewski, R. Naaman, Y. Paltiel, *Science* **2018**, *360*, 1331.

[53] N. Koumura, R. W. J. Zijlstra, R. A. van Delden, N. Harada, B. L. Feringa, *Nature* **1999**, *401*, 152.

[54] **N.d.**

[55] N. Koumura, E. M. Geertsema, A. Meetsma, B. L. Feringa, *J. Am. Chem. Soc.* **2000**, *122*, 12005.

[56] **N.d.**

[57] J. V. Hernández, E. R. Kay, D. A. Leigh, *Science* **2004**, *306*, 1532.

[58] J. Kobayashi, K. Uchino, H. Matsuyama, K. Saito, *Journal of Applied Physics* **1991**, *69*, 409.

[59] A. M. Glazer, K. Stadnicka, *Acta Cryst A* **1989**, *45*, 234.

[60] S. Hoshino, Y. Okaya, R. Pepinsky, *Phys. Rev.* **1959**, *115*, 323.

[61] B. T. Matthias, C. E. Miller, J. P. Remeika, *Phys. Rev.* **1956**, *104*, 849.

[62] E. A. Wood, A. N. Holden, *Acta Cryst* **1957**, *10*, 145.

[63] T. Sekido, T. Mitsui, *Journal of Physics and Chemistry of Solids* **1967**, *28*, 967.

[64] G. L. J. A. Rikken, N. Avarvari, *Nat Commun* **2022**, *13*, 3564.

[65] Y. Terasawa, T. Kikuta, M. Ichiki, S. Sato, K. Ishikawa, T. Asahi, *Journal of Physics and Chemistry of Solids* **2021**, *151*, 109890.

[66] T. Kikuta, D. Hamatake, T. Yamazaki, N. Nakatani, *Ferroelectrics* **2007**, *347*, 65.

[67] M. Trybus, A. Szlachta, *Infrared Physics & Technology* **2022**, *123*, 104211.

[68] B. Göhler, V. Hamelbeck, T. Z. Markus, M. Kettner, G. F. Hanne, Z. Vager, R. Naaman, H. Zacharias, *Science* **2011**, *331*, 894.

[69] V. Kiran, S. P. Mathew, S. R. Cohen, I. H. Delgado, J. Lacour, R. Naaman, *Adv. Mater.* **2016**, *28*, 1957.

[70] M. Kettner, V. V. Maslyuk, D. Nürenberg, J. Seibel, R. Gutierrez, G. Cuniberti, K.-H. Ernst, H. Zacharias, *J. Phys. Chem. Lett.* **2018**, *9*, 2025.

[71] K. S. Kumar, N. Kantor-Uriel, S. Pulinthanathu Mathew, R. Guliamov, R. Naaman, *Physical Chemistry Chemical Physics* **2013**, *15*, 18357.

[72] Z. Xie, T. Z. Markus, S. R. Cohen, Z. Vager, R. Gutierrez, R. Naaman, *Nano Lett.* **2011**, *11*, 4652.

[73] M. Suda, Y. Thathong, V. Promarak, H. Kojima, M. Nakamura, T. Shiraogawa, M. Ehara, H. M. Yamamoto, *Nat Commun* **2019**, *10*, 2455.

[74] N. Koumura, R. W. J. Zijlstra, R. A. van Delden, N. Harada, B. L. Feringa, *Nature* **1999**, *401*, 152.

[75] W. R. Browne, B. L. Feringa, *Nature Nanotech* **2006**, *1*, 25.

[76] M. M. Pollard, M. K. J. ter Wiel, R. A. van Delden, J. Vicario, N. Koumura, C. R. van den Brom, A. Meetsma, B. L. Feringa, *Chemistry – A European Journal* **2008**, *14*, 11610.

[77] R. A. van Delden, M. K. J. ter Wiel, M. M. Pollard, J. Vicario, N. Koumura, B. L. Feringa, *Nature* **2005**, *437*, 1337.

[78] D. H. Waldeck, R. Naaman, Y. Paltiel, *APL Materials* **2021**, *9*, 040902.

[79] B. P. Bloom, V. Kiran, V. Varade, R. Naaman, David. H. Waldeck, *Nano Lett.* **2016**, *16*, 4583.

[80] Y.-H. Kim, Y. Zhai, H. Lu, X. Pan, C. Xiao, E. A. Gaulding, S. P. Harvey, J. J. Berry, Z. V. Vardeny, J. M. Luther, M. C. Beard, *Science* **2021**, *371*, 1129.

[81] D. K. Schwartz, *Annu. Rev. Phys. Chem.* **2001**, *52*, 107.

[82] A. Rumpel, M. Novak, J. Walter, B. Braunschweig, M. Halik, W. Peukert, *Langmuir* **2011**, *27*, 15016.

[83] C. Boulas, J. V. Davidovits, F. Rondelez, D. Vuillaume, *Phys. Rev. Lett.* **1996**, *76*, 4797.

[84] J. Xu, A. Takai, A. Bannaron, T. Nakagawa, Y. Matsuo, M. Sugimoto, Y. Matsushita, M. Takeuchi, *Mater. Chem. Front.* **2018**, *2*, 780.

[85] Q. Zhu, W. Danowski, A. K. Mondal, F. Tassinari, C. L. F. van Beek, G. H. Heideman, K. Santra, S. R. Cohen, B. L. Feringa, R. Naaman, *Advanced Science* **2021**, *8*, 2101773.

[86] R. M. Stöckle, Y. D. Suh, V. Deckert, R. Zenobi, *Chemical Physics Letters* **2000**, *318*, 131.

[87] B. Pettinger, B. Ren, G. Picardi, R. Schuster, G. Ertl, *Phys. Rev. Lett.* **2004**, *92*, 096101.

[88] S. Gidon, O. Lemonnier, B. Rolland, O. Bichet, C. Dressler, Y. Samson, *Appl. Phys. Lett.* **2004**, *85*, 6392.

[89] Y. Tokura, N. Nagaosa, *Nat Commun* **2018**, *9*, 3740.

[90] H. V. Alexandru, C. Berbecaru, L. Ion, A. Dutu, F. Ion, L. Pintilie, R. C. Radulescu, *Applied Surface Science* **2006**, *253*, 358.

[91] H. V. Alexandru, C. Berbecaru, F. Stanculescu, L. Pintilie, I. Matei, M. Lisca, *Sensors and Actuators A: Physical* **2004**, *113*, 387.

List of Publication

R. Malatong, T. Sato*, J. Kumsampao, T. Minato, M. Suda, V. Promarak, H. M. Yamamoto*, Highly Durable Spin Filter Switching Based on Self-Assembled Chiral Molecular Motor. *Small* **2023**, 2302714.